Ocean Modelling 147 (2020) 101565

Contents lists available at ScienceDirect

Ocean Modelling

journal homepage: www.elsevier.com/locate/ocemod

Topographic and coastline influences on surf Eddies

Çiğdem Akan [a,*], James C. McWilliams [b], Yusuke Uchiyama [c]

[a] College of Computing, Engineering, & Construction, University of North Florida, Jacksonville, FL, USA
[b] Department of Atmospheric and Oceanic Sciences, University of California Los Angeles, Los Angeles, CA, USA
[c] Department of Civil Engineering, Kobe University, Kobe, Japan

ARTICLE INFO

Keywords:
Rip current
Surf zone
Instability
Topographic effects

ABSTRACT

Rip currents arise from the momentum flux associated with depth-induced breaking of incident surface gravity waves on beaches with irregular bottom topography. In 3D simulations with an idealized topographic configuration, uniform density, and a steady incident wave field, a striking enhancement of transient surf eddy variability occurs over irregular topography compared to smooth topography, especially at nearly normal incident wave angles. Alternatively, with highly oblique incident waves, transient shear instability is observed over smooth topography whereas for irregular topography, standing rip eddies are generated. In the presence of larger-scale coastline variations, mega-rip circulations emerge, and they are especially strong for embayments. In all cases with significant transient surf-eddy activity, the eddy-induced mean horizontal transport is a non-trivial component of the total mean transport, and sometimes it is much larger than the gravity-wave Stokes drift. Typically the transport by the eddy-induced flow partially cancels the Eulerian transport by the time- and/or alongshore-averaged currents, but not by enough to reverse the "residual" pattern of total transport.

1. Introduction

More than 1/3 of the U. S. population lives in the coastal regions (Crossett et al., 2013). These areas are important for recreational activities, and their popularity is accompanied by beach hazards. One of the leading coastal hazards resulting in surf zone fatalities is rip currents (National Weather Service, 2016). Rip currents are commonly observed as strong and narrow currents moving offshore from the coast and exist generally on beaches with strong surf. They are also important for transporting dissolved and suspended materials across the surf zone.

Alongshore currents and sea-level set-up (*i.e.,* increasing surface height approaching the shore) arise from depth-induced wave breaking (Longuet-Higgins and Stewart, 1962), and rip currents arise due to either current instability, incident wave variability, or topographic variations. Many previous studies concerning rip currents attempt to understand the mechanisms behind their generation and dynamics, *e.g.,* Dalyrmple et al. (2011) or Castelle et al. (2016) are literature reviews on mechanisms for rip current generation. Rip current modeling studies can be divided into two categories: modeling studies accompanied with measurements or laboratory experiments (*e.g.,*Bruneau et al., 2011; Haas et al., 2003; Marchesiello et al., 2015, 2016; Uchiyama et al., 2017); idealized modeling studies (*e.g.,*Yu and Slinn, 2003; Özkan Haller and Li, 2003; Uchiyama et al., 2009; Weir et al., 2011). Idealized rip current studies are mostly performed with alongshore-uniform bathymetries or with added periodic alongshore oscillations, termed rip channels for the offshore flow that forms where the depth is larger. Rip channel spacing and depth has been shown to play a significant role in the strength of the rip currents and on the instabilities (Yu and Slinn, 2003; Castelle et al., 2014). Castelle et al., 2014 showed a decrease in surf zone retention with increasing rip spacing. The incident wave angle is another important factor that with increasing obliqueness intensifies the alongshore current and suppresses the rip current formation. As a result, the surf eddies die out, and the flow becomes more nearly steady when the incident wave field is steady (Yu and Slinn, 2003; Weir et al., 2011). Moreover, field and laboratory measurements (*e.g.,* Haller et al., 2014; MacMahan et al., 2004) reveal energetic very low frequency (VLF) motions correlated with the rip channels. The relation between the topographic irregularities and rip current instabilities (VLF motions) is poorly understood, and this paper further explores it. Another perspective on the origins of VLF currents is that they are associated with alongshore and temporal variability of the incident surface wave field (Feddersen et al., 2011), but this mechanism is not explored here.

Most earlier studies were performed using depth-averaged (2-D) models, but in recent years the importance of the three-dimensionality in modeling rip current systems started to receive more attention (Marchesiello et al., 2015; also see the companion paper by Uchiyama et al. (2017) for a detailed analysis of 2-D versus 3-D simulations for the DUCK experimental site). Study by Uchiyama et al. (2017) also shows vigorous surf eddy activity associated with the topographic irregularities. This motivates the present, more systematic study of this influence

* Corresponding author.
E-mail address: cigdem.akan@unf.edu (Ç. Akan).

https://doi.org/10.1016/j.ocemod.2019.101565
Received 12 March 2019; Received in revised form 16 December 2019; Accepted 26 December 2019
Available online 16 January 2020
1463-5003/Published by Elsevier Ltd.

Table 1
Case list for straight coastlines. θ is the incident wave angle. Note that the case names are coded based on the topography type, smoothness and wave angle. For example, **SB3** would denote the smooth barred topography case with $\theta = 3°$ whereas **IB3** would denote the irregular barred topography case with $\theta = 3°$.

	Topo	θ	Smooth/irregular		Topo	θ	Bathymetry type
SB0	Barred	0°	Smooth	**SP0**	Planar	0°	Smooth
SB3	Barred	3°	Smooth	**SP3**	Planar	3°	Smooth
SB5	Barred	5°	Smooth	**SP5**	Planar	5°	smooth
SB10	Barred	10°	Smooth	**SP10**	Planar	10°	Smooth
SB15	Barred	15°	Smooth	**SP15**	Planar	15°	Smooth
SB20	Barred	20°	Smooth	**SP20**	Planar	20°	Smooth
SB25	Barred	25°	Smooth	**SP25**	Planar	25°	Smooth
SB30	Barred	30°	Smooth	**SP30**	Planar	30°	Smooth
SB35	Barred	35°	Smooth	**SP35**	Planar	35°	Smooth
SB40	Barred	40°	Smooth	**SP40**	Planar	40°	Smooth
IB0	Barred	0°	Irregular	**IP0**	Planar	0°	Irregular
IB3	Barred	3°	Irregular	**IP3**	Planar	3°	Irregular
IB5	Barred	5°	Irregular	**IP5**	Planar	5°	Irregular
IB10	Barred	10°	Irregular	**IP10**	Planar	10°	Irregular
IB15	Barred	15°	Irregular	**IP15**	Planar	15°	Irregular
IB20	Barred	20°	Irregular	**IP20**	Planar	20°	Irregular
IB25	Barred	25°	Irregular	**IP25**	Planar	25°	Irregular
IB30	Barred	30°	Irregular	**IP30**	Planar	30°	Irregular
IB35	Barred	35°	Irregular	**IP35**	Planar	35°	Irregular
IB40	Barred	40°	Irregular	**IP40**	Planar	40°	Irregular

on surf eddies. Here we present results from idealized simulations using the three dimensional (3-D) ROMS-WEC model (Uchiyama et al., 2010) to explore the role of complex, small-scale bathymetry in instigating very low frequency (VLF) currents that are highly turbulent and eddy-like, in contrast to currents over a smooth, alongshore-uniform bathymetry. Further, we examine the effects of shoreline bays and headlands on wave-driven currents.

In Section 2 we describe the modeling approach and the stochastic perturbation method used to generate different topographies. Results from numerical simulations with and without complex bathymetry are presented in Section 3. In Section 4, the role of the coastline shape and its interaction with rip currents are explored. Summary and discussion of the results are in Section 5.

2. Methods

2.1. The ROMS-WEC model

A total of 52 cases (plus additional sensitivity tests in the Appendices) are performed using the coupled ROMS-WEC model, *i.e.,* the Regional Oceanic Modeling System with Wave Effects on Currents (Uchiyama et al., 2010). Lists of the cases are in Tables 1–2 and the Appendices. The model consists of the circulation model ROMS and a spectrum-peak, finite-depth wave model (*i.e.,* WKB ray theory with a depth- and current-induced refraction, and a depth-induced breaking, and a bottom-drag wave dissipation parameterization). The Stokes drift is calculated from the WKB wave solution, and the current acceleration is parameterized from the wave dissipation rates by surface breaking and by bottom drag. The model is fully-coupled with surface gravity wave effects on currents (WEC) and current effect on the waves (CEW) based on the conservative asymptotic theory developed by McWilliams et al. (2004) and the non-conservative model implementation by Uchiyama et al. (2010).

Periodicity is assumed in the alongshore direction. At the offshore open boundary, we assume no net outflow by the sum of the Eulerian current and Stokes drift. At the western shoreline a wall boundary condition is applied with a minimum depth of 0.1 m, and wetting and drying behaviors are excluded. In practice bottom drag and depth-induced breaking make the waves and currents nearly zero in such shallow water near the shoreline. The Coriolis force is neglected because the Rossby number is very large for littoral currents and surf eddies. The water density is uniform.

Table 2
Case list for variable coastlines. θ is the incident wave angle. For example, **H5** would denote the headland case with $\theta = 5°$ whereas **B5** would denote the bay case with $\theta = 5°$.

	Coast shape	θ		Coast shape	θ
H0	Headland	0°	**B0**	Bay	0°
H5	Headland	5°	**B5**	Bay	5°
H10	Headland	10°	**B10**	Bay	10°
H20	Headland	20°	**B20**	Bay	20°
H30	Headland	30°	**B30**	Bay	30°
H40	Headland	40°	**B40**	Bay	40°

For the primary cases in Tables 1–2, the only forcing is by incident steady, monochromatic waves specified at the offshore boundary with a wave amplitude of $a = 0.5$ m and a peak wave period $T_p = 10$ s; *i.e.,* there is no wind forcing, no heating, and no river inflow. The incident wave angle θ is varied among cases. Additional sensitivity tests are performed varying a while keeping the offshore incident angle θ and wave period T_p constant Appendix C. The depth-induced wave-breaking parameterization proposed by Thornton and Guza (1983) is used:

$$\epsilon_b = \frac{3\sqrt{\pi}}{16}\,\frac{\rho g f_p \beta^3 H_{\rm rms}^5}{\gamma^2 h^3}\left(1-\left(1+\left[\frac{H_{rms}}{\gamma h}\right]^2\right)^{-5/2}\right)^{-1}, \tag{1}$$

$H = h + \eta_c$ is the local water-column thickness, where h is the still water depth and $\eta_c = \eta + \hat{\eta}$ is the wave-averaged surface elevation that is the sum of the dynamic sea level and the quasi-static response due to the conservative wave effects on the currents (WEC) (Uchiyama et al., 2010), g is gravitational acceleration, ρ is the oceanic density, γ is the maximum ratio of wave height to water depth, f_p is the peak frequency of the narrow band wave energy spectrum, β is a factor representative of the level of energy dissipation, and $H_{\rm rms} = H/\sqrt{2}$ is the root-mean-square wave height.

Previous studies show that different wave breaking parameterizations can give different results, and they are sensitive to changes in the significant wave height, H_s. In realistic applications the parameters γ and β are tuned in to fit the observations. In our idealized cases, we use a universal form of γ as proposed by Apotsos et al. (2008) while choosing $\beta = 1$,

$$\gamma = A + B[\tanh(C H_o)], \tag{2}$$

where H_o is the offshore wave height, $A = 0.18$, $B = 0.40$, and $C = 0.90$ for the parameterization (1). The bottom stress is an important element of a surf-zone model, and there is a wide variety of representations used in the literature. For our idealized study, we choose a particular representation and keep it the same as the topography is varied. The nonlinear parameterization of bottom stress proposed by Feddersen et al. (2000) is used:

$$\boldsymbol{\tau}_b = \rho c_D \left[(1.16)^2 + \left(\frac{|\mathbf{u_b}|}{u_{rms}^{wv}}\right)^2\right]^{1/2} u_{rms}^{wv}\,\mathbf{u_b}, \tag{3}$$

where C_D is the bottom friction coefficient equal to 0.01, u_{rms}^{wv} is the root mean square wave orbital velocity, and $\mathbf{u_b} = (u_b, v_b)$ is the bottom current velocity. We tested different bottom stress parameterizations found in the literature including linear, quadratic, logarithmic, and one proposed by Soulsby (1995) that also includes combined effects of waves and currents. The linear and quadratic bottom stress parameterizations generate more instabilities compared to the logarithmic bottom stress parameterization and parameterizations proposed by Soulsby (1995) and Feddersen et al. (2000). We also found that Soulsby (1995) suppresses littoral current instabilities much more than (3) does. Lateral momentum diffusion is included with $\nu = 1$ m^{2}s^{-1} (but see Appendix E).

All cases are initialized at rest with a flat sea level and no waves inside the domain. They are integrated forward in time to a statistical steady state that is then analyzed for the results in Sections 3–4.

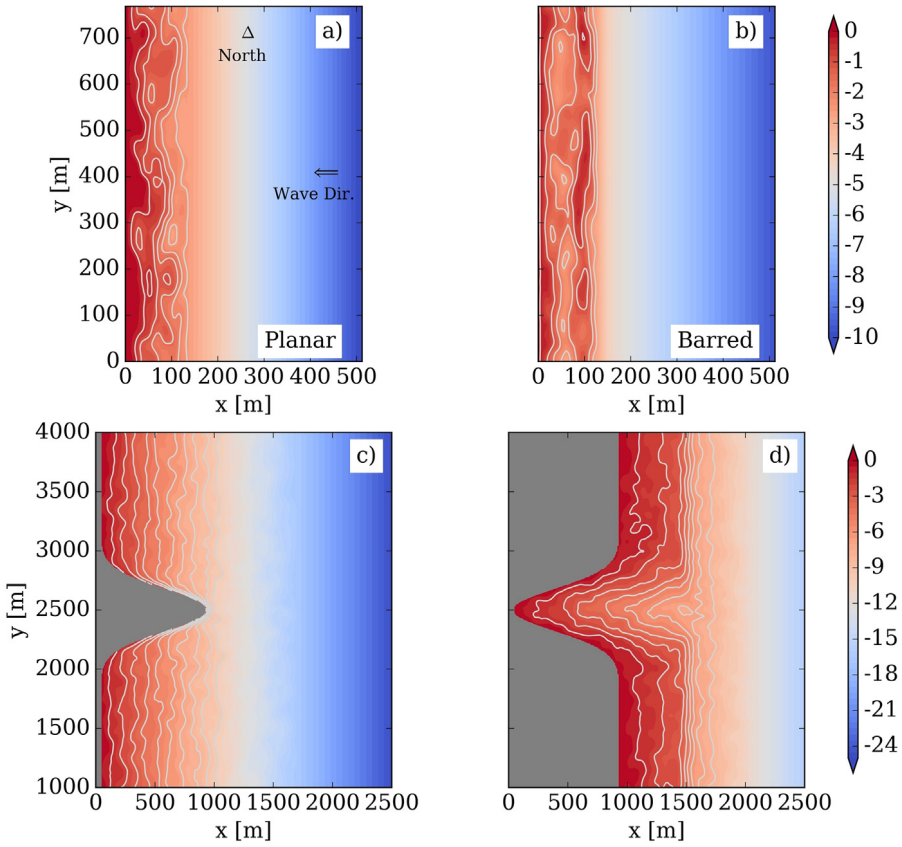

Fig. 1. Maps of the irregular (a) planar, (b) barred, (c) headland, and (d) bay topographies. Colormaps show the depth, and contour lines accentuate the variations. In all cases the topographic perturbation height pL_z is the same, but the domains are wider and longer in (c) and (d), and the total depth range is larger.

2.2. Topographies

Most idealized rip current studies are carried out with alongshore-uniform or -periodic topographies where parameters such as incident wave angle and bottom friction coefficient, are varied to identify the relevant alongshore flow and rip current generation mechanisms. Commonly used topographies are alongshore-uniform barred topography (*e.g.,* Özkan Haller and Li, 2003; Uchiyama et al., 2009) and barred topography with uniformly spaced channels (*e.g.,* Yu and Slinn, 2003; Weir et al., 2011; Xie, 2011). Here, we make a more complete examination of the role of the more complex alongshore irregularities in the topography in rip currents.

The first set of simulations listed in Table 1 is divided into two main groups; "smooth" and "irregular" where "smooth" means alongshore-uniform topography and "irregular" means smooth topography combined with stochastic depth variations, as explained below. The alongshore averages of the smooth and irregular topographies are the same. To illustrate the irregularities, we show two simple domains with straight coastlines in the top panels of Fig. 1: panel (a) is an irregular planar beach topography (*i.e.,* with a uniform bottom slope in the alongshore average), and panel (b) is the irregular barred topography (*i.e.,* with an isolated bump at an intermediate distance from the shoreline), whose smooth counterpart is the same as in the study by Özkan Haller and Li (2003). The size of these domains is 512 m by 768 m with $dx = dy = 4$ m horizontal resolution, and there are 20 terrain-following layers in the vertical direction. Cases with these topographies are analyzed in Section 3.

In the second set of simulations in Table 2, we explore the influence of the shape of the coastline in generating and interacting with the currents (Section 4). Two different coastline configurations are generated with either a headland or a bay, as illustrated in Fig. 1c, d. The size of the headland and bay domains is larger to accommodate the range of coastline orientations, *i.e.,* 5000 m by 5000 m with $dx = dy = 10$ m grid resolution and 20 terrain-following layers.

Table 3
Perturbation cross-shore width (pL_x), alongshore length (pL_y), amplitude (pH) and the offshore limit of the perturbations x_{osd} for different cases.

	pL_x	pL_y	pH	x_{osd} [m]
Planar	80 m	80 m	0.5	Lx/4
Barred	80 m	80 m	0.5	Lx/4
Headland	100 m	100 m	0.5	Lx/3
Bay	100 m	100 m	0.5	Lx/3

Irregular topography is composed of an alongshore-uniform topography superimposed with random depth perturbations. To generate stochastic perturbations, the procedure described by Evensen (2007) is followed. This method generates random depth fields $h'(x, y)$ with prescribed characteristics: $\mu = 0$ is the mean, $\sigma^2 = pH^2$ is the variance, and the horizontal covariance function is

$$C_{hh}(\Delta x, \Delta y) = pH^2 \exp\left(-\frac{\Delta x^2}{pL_x^2} - \frac{\Delta y^2}{pL_y^2}\right), \tag{4}$$

where Δx and Δy are spatial separation distances, pL_x is the spatial scale of the perturbations in the cross-shore direction, pL_y is the spatial scale of the perturbations in the alongshore direction, and pH is the perturbation amplitude. The size and amplitude of the perturbations (pL_x, pL_y, pH) are to be specified. For the present study, we have chosen pL_x, pL_y and pH values such that random rip channels are generated at realistic vertical and lateral scales (see Table 3 for the values used).

Thus, the perturbed topographic depth is defined by

$$h(x, y) = h_0(x, y)\left[1 + s_0\, h'(x, y)\right], \tag{5}$$

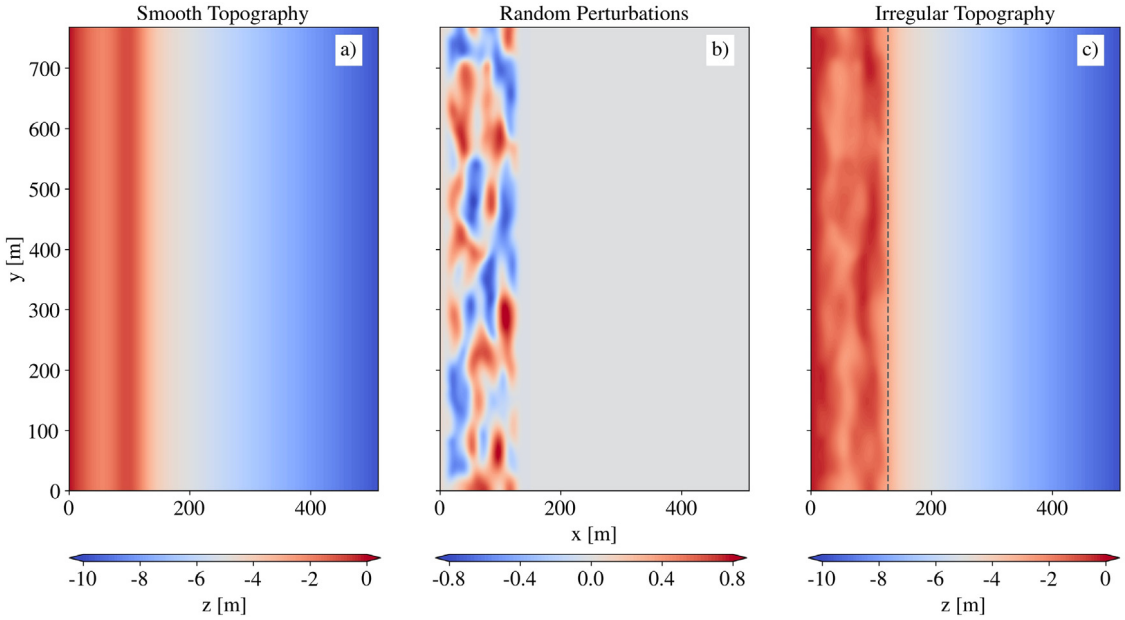

Fig. 2. Map illustrating the topographic components [m]: (a) smooth barred topography $h_0(y)$, (b) random perturbations $h'(x, y)$, and (c) irregular total topography $h(x, y)$. The dashed line in panel (c) indicates the location of x_{osd}.

where $h_0(x, y)$ is the smooth topography, s_0 is a roughness control parameter ($s_0 \in [0, 1]$) whose sensitivity is examined in Appendix C, and $h'(x, y)$ is the non-dimensional random depth field. The sensitivity to particular realizations for h' is examined in Appendix A. The offshore extent of the perturbations is limited on a scale that is slightly larger than the surfzone width, x_{osd}, to prevent artificial effects close to the offshore boundary; its value for different cases is also listed in Table 3. Then local smoothing is applied near $x = x_{osd}$ to assure that h is continuous. The factor r_{max}, maximum grid stiffness factor, is less than 0.35 for all the perturbed cases. Also, the topography close to the shoreline is kept the same for both smooth and irregular cases. This is determined by setting up a distance limit similar to the offshore limit, but for a much shorter distance, i.e. the depth is set to minimum depth from shoreline to $x = 16$ m. This prevented the occurrence of steep bathymetry close to the shoreline. All the runs listed in Tables 1 and 2 are carried out with $s_0 = 1$. We illustrate the composition of irregular topography using the preceding method in Fig. 2. Panel (a) is the smooth barred topography $h_0(y)$, panel (b) is a random realization for $h'(x, y)$, and panel c is the combined total topography $h(x, y)$.

For headland and bay cases, we first examined the bathymetry around several headlands and bays found in the nature. In our observations the topography around most headlands deepens sharply compared to the beach bathymetries adjacent to it whereas the topography within most bays has a milder slope. Moreover, the study by George (2016) investigated circulation and sediment transport at headlands and by doing so he categorized different headlands in the California coast. Appendix 1 of that study presents a database of classified headlands. The size of the headland (perimeter) used in the present modeling work is consistent with most the headlands listed in the aforementioned database. The bay used in the study is just the symmetric inverse of the headland, but as will be explained in Section 4, it generates mega-rips similar to the one observed around a submarine canyon off La Jolla, CA, near the Scripps Research Pier (Long and Özkan Haller, 2005).

Thus, we construct smooth topographies $h_0(x, y)$ of the headland and bay domains accordingly, then add the random field $h'(x, y)$, and again limit its offshore extent. The smooth topography in these cases does not have an offshore bar.

3. Effects of irregular topography

This section analyzes the cases with a straight shoreline and demonstrates the differences between smooth and irregular topographies. If the alongshore-uniformity of h is broken, *e.g.,*by adding rip channels, then offshore-directed rip currents will form, both steady and transient (Section 1). To trigger flow instabilities, small perturbations (*i.e.,* random noise in the order of 10^{-5} [m s^{-1}]) are sometimes added to the velocity field at an early time but after currents have arisen. In our irregular bathymetry cases, we do not need to add perturbations to the velocity field because the instabilities develop almost from the beginning with all incident wave angles. However, with increasing θ, the instabilities are suppressed. We define a surf eddy as a deviation of vorticity from an alongshore-average within the nearshore region, and eddies can be either time-varying (transient) or steady in time (standing). Note that identification of the eddies was done visually where we consider an eddy as a closed circulation.

As an illustration of the current field, Fig. 3 shows the instantaneous surface vertical vorticity for smooth and irregular barred cases with alternative wave incident angles $\theta = 0°$ (top panels) and $\theta = 40°$ bottom panels) at the end of the simulation (at the 12th hour of integration). Surf eddies do not develop in the smooth case when the waves are normally incident; in other words, having a smooth alongshore-uniform topography does not generate any appreciable currents, so there is no possible instability for their generation. With irregular topography, however, currents do develop and become unstable due to their horizontal shear, and the resulting surf eddies are nearly isotropic in their horizontal pattern (Fig. 3b). If the waves are obliquely incident, then an alongshore current arises from the breaking-wave acceleration and horizontal shear instabilities ensue (Fig. 3c). With irregular topography the surface vertical vorticity is enhanced for obliquely incident waves, but the current instability is suppressed: the surf eddies are now almost entirely steady in time, *i.e.,* standing eddies rather than transient ones (Fig. 3d). The sensitivity test in Appendix B shows that with a somewhat lowered bar height, transient eddies still occur with irregular topography and large θ, albeit still weaker than the standing eddies in that regime.

3.1. Eddy kinetic energy (EKE)

We quantify surf eddy activity with the time-averaged eddy kinetic energy EKE. We decompose the fields into time-averaged and transient-eddy components, $\phi = \bar{\phi} + \phi'$, where an overbar denotes time averaging, a prime denotes deviation from the time average. A

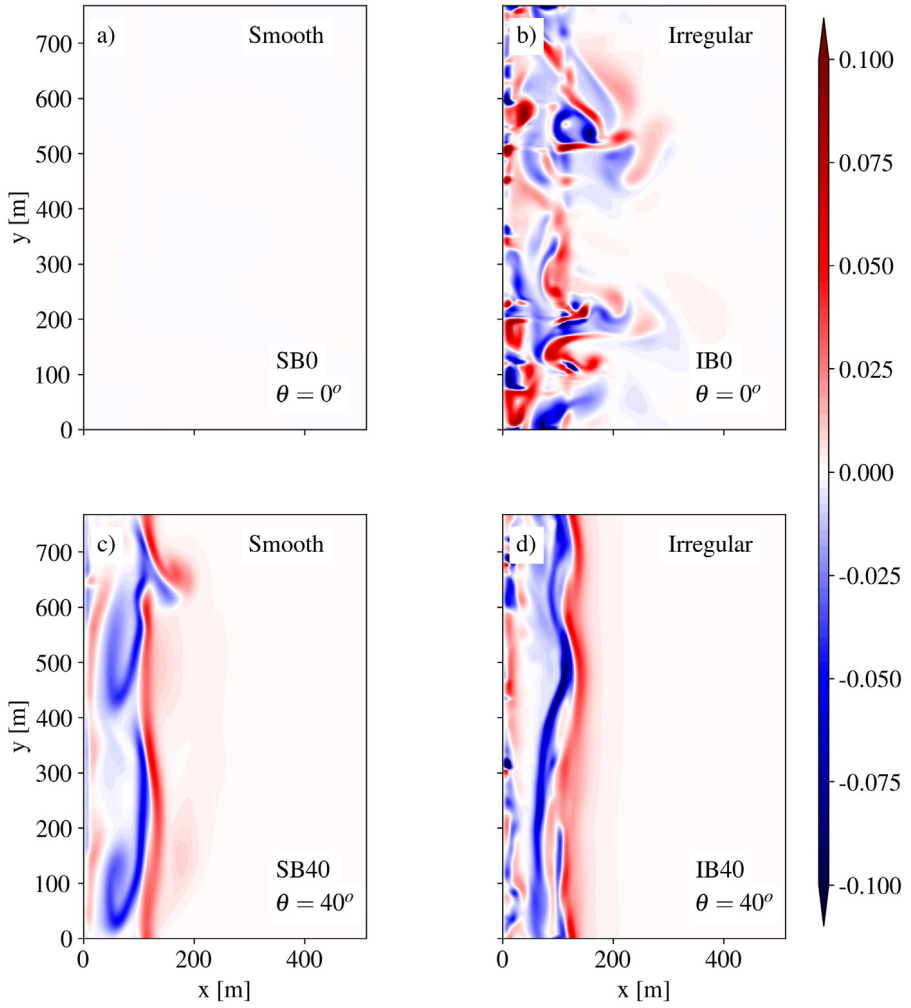

Fig. 3. Instantaneous surface vertical vorticity $\zeta^s_z(x, y)$ [s^{-1}] at the 12th hour of the simulation for (a) smooth barred topography with $\theta = 0°$ (SB0), (b) irregular barred topography with $\theta = 0°$ (IB0), (c) smooth barred topography with $\theta = 40°$ (SB40), and (d) irregular barred topography with $\theta = 40°$ (IB40). Parameters for the cases are in Table 1. The currents in panel (a) are too weak to be seen with this colorbar.

further decomposition of $\bar{\phi}$ can be made into an alongshore-averaged component, $\langle\bar{\phi}\rangle$, and its standing-eddy deviation, $\phi^s = \bar{\phi} - \langle\bar{\phi}\rangle$, where angle brackets denote the alongshore average.[1] Thus, the total field is

$$\phi = \langle\bar{\phi}\rangle + \phi^s + \phi' \,, \tag{6}$$

and $\phi^s + \phi'$ is the total eddy component. Furthermore, the time- and alongshore-averaged variance is

$$\langle\overline{\phi^2}\rangle = \langle\bar{\phi}\rangle^2 + \langle\phi^{s\,2}\rangle + \langle\overline{\phi'^2}\rangle \,. \tag{7}$$

The first right-side term in (7) is the variance of the mean, and the second and third terms are the variances of the standing and transient eddies, respectively.

This decomposition is applied to the velocity and then depth-integrated and multiplied by $\frac{1}{2}$ to calculate mean, standing-eddy, and transient eddy kinetic energies. 3-D velocity vectors are $(\mathbf{u}, w)$, where $\mathbf{u} = (u, v)$ is the velocity vector in the horizontal direction and w is the velocity in the vertical direction. The total eddy kinetic energy EKE is the sum of the standing and transient components. Steady rip currents would contribute through the standing EKE.

Fig. 4 shows clearly that irregular barred topography is highly energetic even when the waves are normally incident (solid black line).[2] For normally and slightly oblique waves, the transient eddy component makes up about one-half of the total EKE. This indicates generation of energetic eddies due to the irregularities in the topography. As the incident wave angle increases, transient eddies start to disappear and standing eddies dominate (compare the solid blue line versus solid red line).

In contrast, because there is not a mean current to generate instabilities, the EKE is almost zero for smooth topography for normal and near normal incident wave angles (dashed black line). With increasing incident wave angle, the transient eddy component increases due to shear instabilities (dashed red line) while the standing eddy component is zero apart from finite-time sampling error. Thus, we conclude that the dominant EKE components change between alongshore-uniform and irregular topographies.

Similar behaviors occur in the planar beach cases (Fig. 5). Even though depth-induced breaking occurs with the same total wave dissipation, hence with the same total current acceleration, it is more

[1] With a variable h the only meaningful alongshore average of a 3D field is one at constant (x, y), the terrain — a free-surface following coordinate in ROMS, rather than one at constant z that would multiply intersect the bottom.

[2] For EKE and the shear production terms P in (9)–(10), we compute 3D fields with time averages, then depth integrate using the mean surface height for wave-averaged currents, $\bar{\eta}_c(x, y)$, and, where indicated, take an additional alongshore- or area-average. This procedure overlooks an additional nonlinearity in averages associated with the variable $\eta_c' = \eta_c - \bar{\eta}_c$. This neglected effect is small in both quantities.

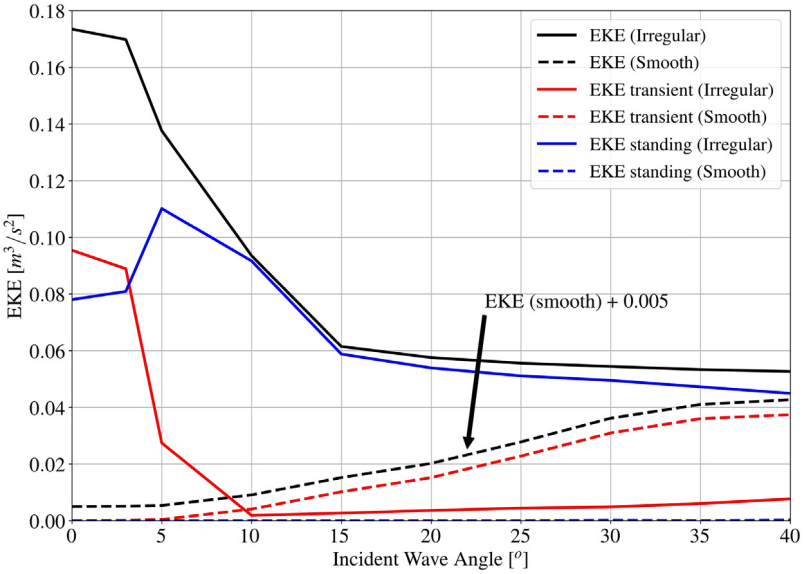

Fig. 4. Total (black), standing (blue), and transient (red) EKE components [m^3 s^{-1}] for smooth (dashed lines) and irregular (solid lines) barred topographies as a function of offshore wave incident angles. EKE is depth-integrated and then horizontally averaged. The EKE for smooth topography and small θ is $\approx 10^{-5}$ [m^3 s^{-1}]. Because the dashed black and the dashed red lines are indistinguishably close to each other, a small displacement is added to make both lines noticeable. The standing EKE for smooth topography (blue dashed line) is zero. (Cases SB1-10 and IB1-20 in Table 1).

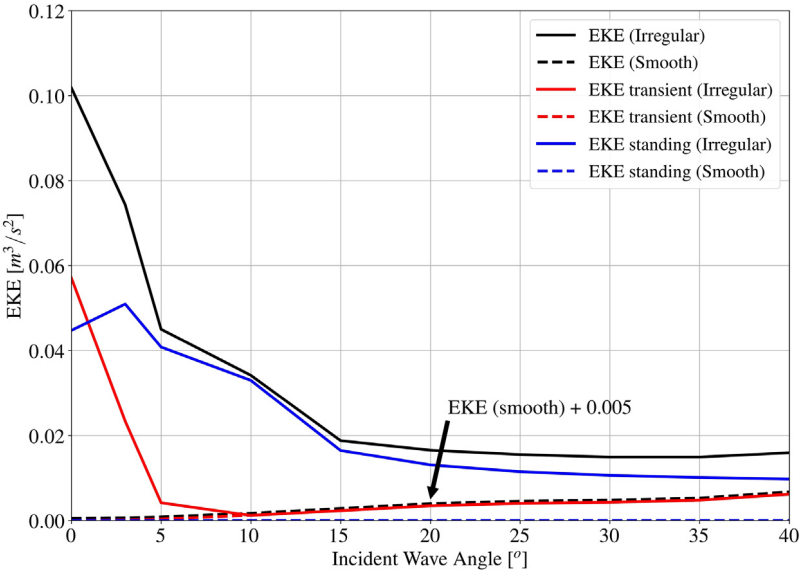

Fig. 5. Total (black), standing (blue), and transient (red) EKE components [m^3 s^{-1}] for smooth (dashed lines) and irregular (solid lines) planar beach topographies as a function of offshore wave incident angles. EKE is depth-integrated and then horizontally averaged. The EKE for smooth topography and small θ is $\approx 10^{-5}$ [m^3 s^{-1}]. Because the dashed black and the dashed red lines are indistinguishably close to each other, a small displacement is added to make both lines noticeable. The standing EKE for smooth topography (blue dashed line) is zero. (Cases SB1-10 and IB1-20 in Table 1).

spatially diffused on a planar beach, so the currents are broader and weaker, compared to the depth-induced breaking with smooth barred topography. Thus, the kinetic energy generated due to depth-induced breaking is also much smaller. The EKE values for the irregular planar beach topography is similar to the one for irregular barred topography but somewhat weaker. Notice that the planar smooth topography does not generate shear waves.

In all these solutions there is an important dependency on the bottom drag, both its functional form and the amplitude of its coefficient, and thus the drag parameterization is an important element of surf zone modeling. We chose not to make this a focus of this paper; refer to Uchiyama et al. (2009, Sec. 4) to learn more about the bottom-drag parameterization dependency.

3.2. Alongshore-averaged current

Previous studies have shown that the Stokes drift $\mathbf{u}^{st}$ tends to cancel the Eulerian velocity in the inner shelf (Fewings et al., 2008). However, this is not always true, resulting in a non-zero Lagrangian velocity,

$$\mathbf{u}^L = \mathbf{u} + \mathbf{u}^{st}. \tag{8}$$

Cross-shore profiles of the depth- and time- and alongshore-averaged Eulerian and Lagrangian velocities and Stokes drift are in Fig. 6. These include both irregular (solid lines) and smooth (dashed lines) barred topographies. The Eulerian cross-shore velocities $\langle \bar{u} \rangle$ are close to each other for all cases shown with the exception of SB40 and IB40 where $\theta = 40°$, the maximum angle examined. Eulerian velocities

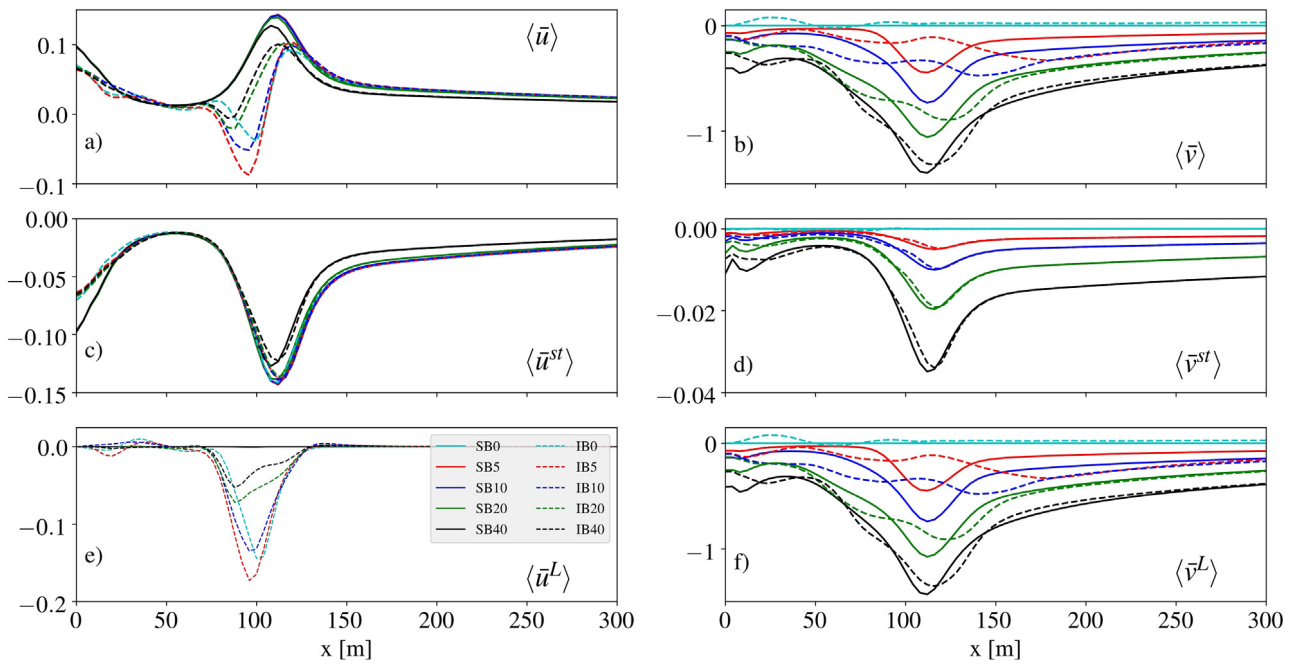

Fig. 6. Cross-shore profiles of depth-, time-, and alongshore-averaged velocities [m s^{-1}]: (a) $\langle \bar{u} \rangle$, (b) $\langle \bar{v} \rangle$, (c) $\langle \bar{u}^{st} \rangle$, (d) $\langle \bar{v}^{st} \rangle$, (e) $\langle \bar{u}^{L} \rangle$, and (f) $\langle \bar{v}^{L} \rangle$. These are all for barred topographies; the smooth topography cases have solid lines, and the irregular have dashed ones (Table 1). The nonzero $\langle u^{L} \rangle$ is balanced by the eddy-induced velocity to have zero total mean Lagrangian cross-shore transport (Section 3.5).

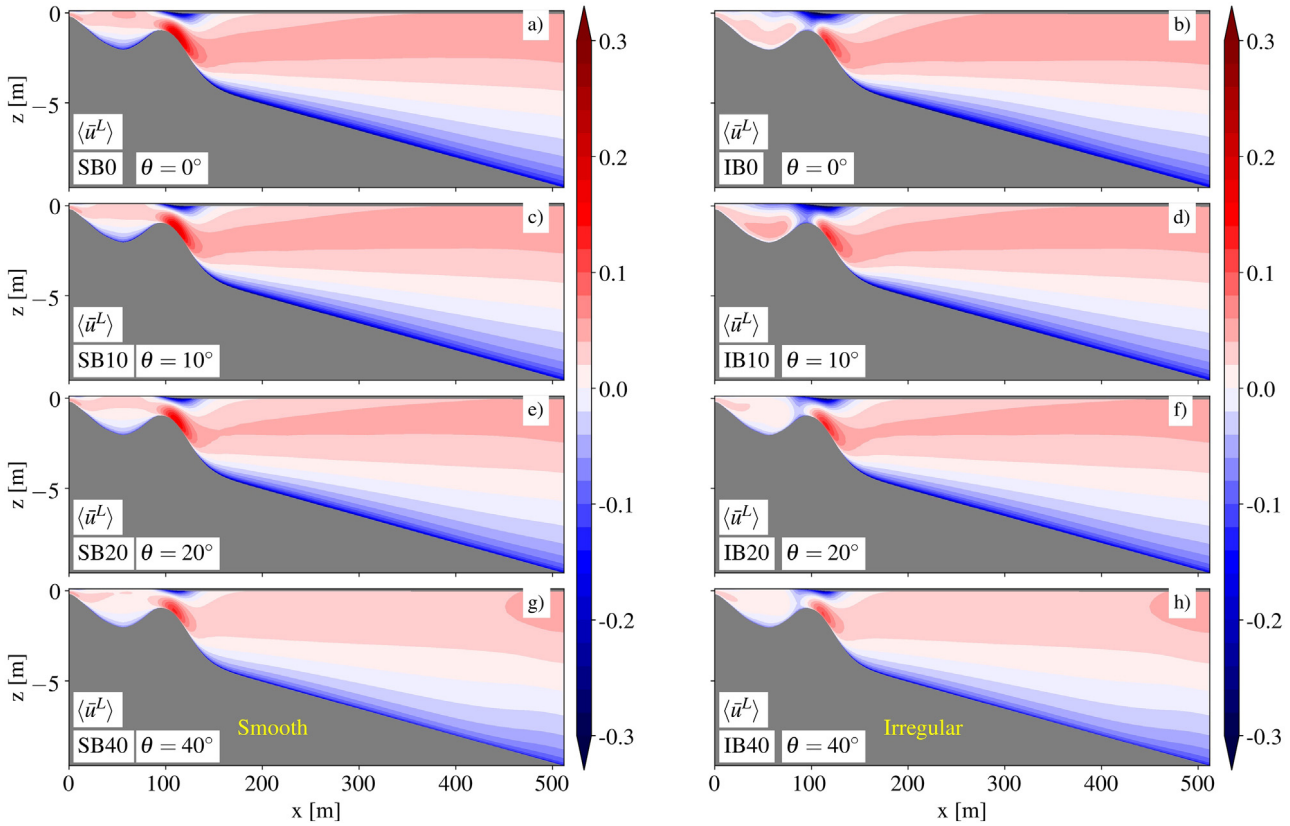

Fig. 7. Cross-shore sections of time- and alongshore averaged Lagrangian velocity in the cross-shore direction, $\langle \bar{u}^{l} \rangle$ [m s^{-1}]. Smooth barred topography cases are in the left column and irregular ones are in the right column (Table 1).

in the alongshore direction $\langle \bar{v} \rangle$ differ significantly between irregular and smooth cases with $\theta < 10°$, but then became more similar at highly oblique incident angles. In the x-far field $\langle \bar{v} \rangle$ decreases somewhat slowly and has an appreciable amplitude for oblique waves. This is due to the bottom-drag wave dissipation that in turn provides an along-wave acceleration of the current at the bottom (Uchiyama et al., 2010); it persists as far offshore as the wave orbital velocity reaches to the bottom. We performed sensitivity studies (not shown) and found that

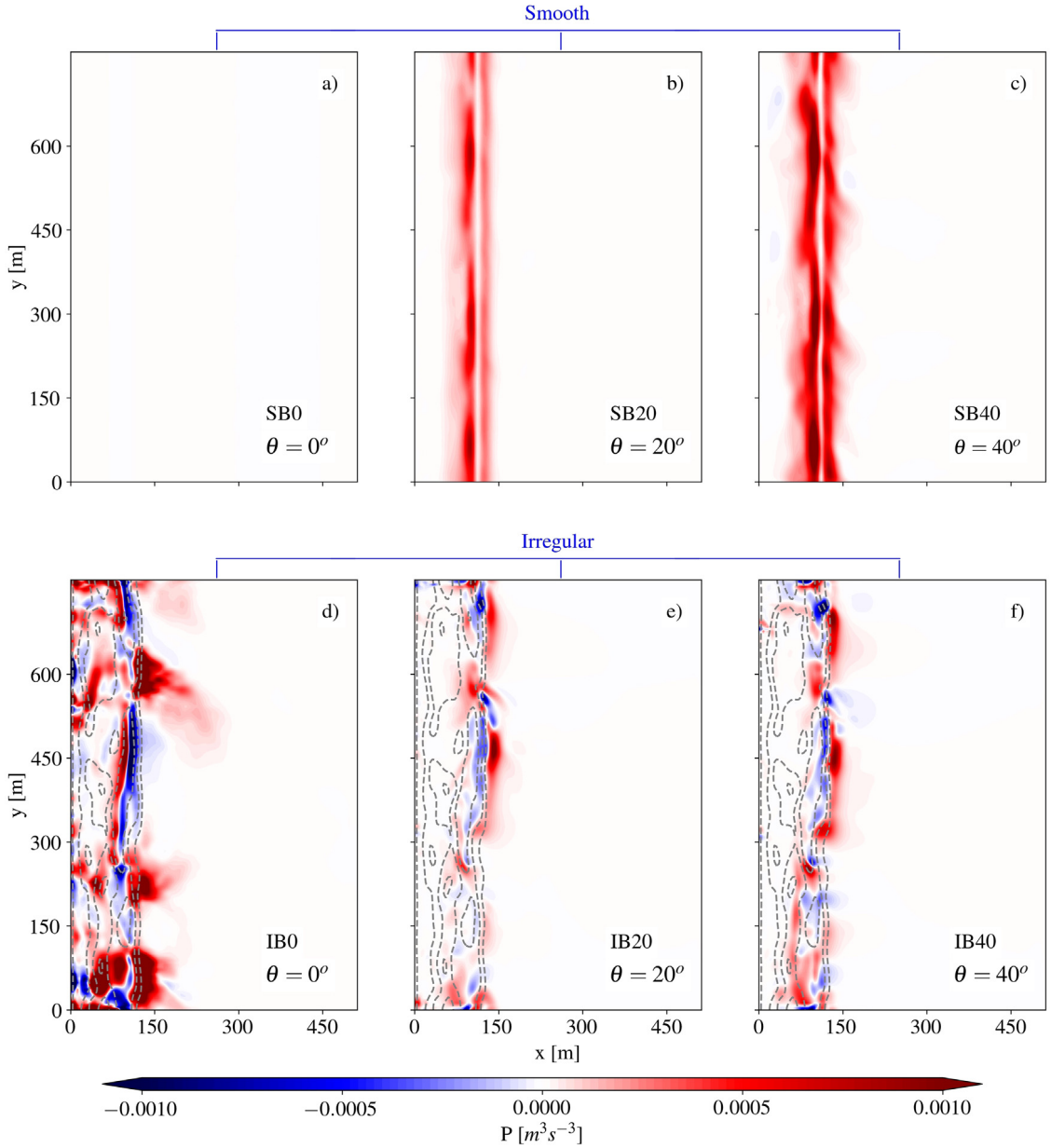

Fig. 8. Maps of time-averaged and depth-integrated horizontal Reynolds stress transient kinetic energy production $P_{M+S\to T}$ [m^3 s^{-3}] for smooth (top panels) and irregular (bottom panels) barred topographies. The upper-left case has no $P_{M+S\to T}$ because it has no transient-eddy EKE (Fig. 4).

the alongshore current in the offshore region is quite sensitive to the particular functional form of this wave bottom-drag parameterization, even though the behavior around the surf zone is robust. This parameterization gives rise to "bottom streaming" currents. More research is needed on whether its prescriptions are accurate.

Stokes drift in the cross-shore direction $\langle \bar{u}^{st} \rangle$ has the same order of magnitude as the mean Eulerian velocity $\langle \bar{u} \rangle$. However, the resulting $\langle \bar{u}^L \rangle$ is almost as large in the smooth topography cases, but smaller than the irregular ones. $\langle v^{st} \rangle$ is relatively small though variable among the cases, in particular between irregular and smooth topographies, so $\langle \bar{v}^L \rangle \approx \langle \bar{v} \rangle$, which itself is quite different among the cases. Although not shown, the mean Lagrangian cross-shore depth-integrated transport $\langle \bar{U}^L \rangle$, defined in (12), is essentially zero, as it should be in an equilibrium state.

Cross-shore sections of $\langle \bar{u}^L \rangle$ for irregular and smooth barred topographies are in Fig. 7. The pattern of u^L is dominated by the Eulerian rip currents. In all cases the dominant pattern is a shoreward surface current accompanied by an offshore flow at depth (undertow) above and just outside the bar. This primary overturning circulation is strongest for normal and slightly oblique angles in both smooth and irregular topographies. Near the bar there is a weak reverse overturning circulation that is stronger with smooth topography and smaller θ. In the offshore region, the bottom flow is shoreward because of bottom streaming associated with the shoreward waves (Section 3.2), with a compensating offshore flow above to achieve a zero depth integral.

3.3. Eddy-mean kinetic energy conversion

The overall energy cycle for surf currents is a kinetic source from the acceleration due to wave breaking and a sink primarily due to bottom drag, although lateral momentum diffusion also contributes. There is an exchange with potential energy as well due to the free surface elevation, but it is secondary compared to the kinetic energy cycle. The mean currents can be unstable and convert mean to eddy kinetic energy, and then the eddies can be an important route to total current dissipation.

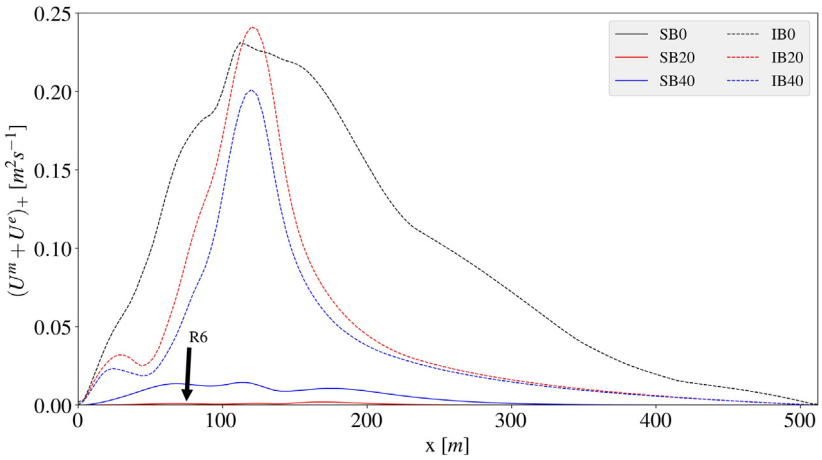

Fig. 9. Rip transport: alongshore-average of the offshore-directed parts of the time-averaged and depth-integrated cross-shore transport, $(U^m + U^e)_+$ [m^2 s^{-1}] for barred topographies: smooth (solid lines) and dashed (dashed). Only the cases with angles of $\theta = 0°$, $20°$, $40°$ are included here (Table 1). Notice that the smooth cases SB0 and SB20 have very weak offshore-directed mean flows.

To assess the energy conversion from time-mean kinetic energy to transient EKE, we calculate the horizontal shear production term $P_{M+S\to T}$, whose integrand is the product of eddy Reynolds stress and mean horizontal shear,

$$P_{M+S\to T} = -\overline{u'u'}\,\frac{\partial \bar{u}}{\partial x} - \overline{u'v'}\,\frac{\partial \bar{v}}{\partial x} - \overline{v'v'}\,\frac{\partial \bar{v}}{\partial y} - \overline{u'v'}\,\frac{\partial \bar{u}}{\partial y}\,, \tag{9}$$

with a further integration over the depth [m^3 s^{-3}]. The subscript notation for P in (9) is based on the energy decomposition implied in (7): it is a conversion from the total time-averaged flow (i.e., the sum of the alongshore mean (M) and standing-eddy (S) components) to the transient-eddy (T) component. A positive sign of P means kinetic energy conversion from the time-mean flow to the transient fluctuations, *i.e.,* transient eddy generation. A two-signed pattern indicates mixed eddy-mean energy conversion with an implication of spatial transport connecting the two regions. The horizontal average of P determines the net conversion [m^5 s^{-3}] (Table 4).

The $P_{M+S\to T}$ term for different cases is shown in Fig. 8. Recall from Fig. 1, which shows the horizontal view of the domains used, that for this particular irregular topographic realization there are three rip channels with varying widths located at around 80 m, 200 m and 600 m, respectively. The largest $P_{M+S\to T}$ conversion coincides with these channels (Fig. 8d) at $\theta = 0°$. As anticipated, with rip currents there are regions of mixed sign for P. As the incident wave angle increases, the magnitude of the $P_{M+S\to T}$ decreases, although it remains significant for all θ. In contrast, with smooth topography $P_{M+S\to T}$ is nearly zero for normal-incident waves and it increases with θ. $P_{M+S\to T}$ reaches a similar magnitude at $\theta = 40°$ as in the irregular cases, even though its total EKE is less (Fig. 4). This is the expected signature of transient shear instability of the alongshore current. It is nearly uniform alongshore. In all cases P is mostly confined to the bar region, although it does reach inside the bar as well in the case with normal incidence over irregular topography. After taking a y-average, $P_{M+S\to T}$ is positive for almost all x values in all cases; this is reflected in the positive area-integrated values in the first row of Table 4.

We can also consider other mean-eddy conversions as defined in these alternative shear production terms:

$$\begin{aligned} P_{M\to S} &= -u^s u^s\,\frac{\partial \langle \bar{u}\rangle}{\partial x} - u^s v^s\,\frac{\partial \langle \bar{v}\rangle}{\partial x} \\ P_{M\to S+T} &= -(\overline{u'u'} + u^s u^s)\,\frac{\partial \langle \bar{u}\rangle}{\partial x} - (\overline{u'v'} + u^s v^s)\,\frac{\partial \langle \bar{v}\rangle}{\partial x} \\ P_{S\to T} &= -\overline{u'u'}\,\frac{\partial u^s}{\partial x} - \overline{u'v'}\,\frac{\partial v^s}{\partial x} - \overline{v'v'}\,\frac{\partial v^s}{\partial y} - \overline{u'v'}\,\frac{\partial u^s}{\partial y}\,, \end{aligned} \tag{10}$$

whose meanings are evident in their different subscripts.

The total magnitudes of these various shear production terms are listed in Table 4. Using the language of horizontal shear instability, they indicate the following energy pathways:

Table 4
Horizontal Reynolds stress (HRS) (9)–(10) [m^5 s^{-3}] integrated over depth and area, and averaged in time for smooth and irregular barred topographies.

	SB0 (0°)	SB20 (20°)	SB40 (40°)	IB0 (0°)	IB20 (20°)	IB40 (40°)
$P_{M+S\to T}$	0.027	13.40	27.38	22.65	4.17	4.93
$P_{M\to S+T}$	0.027	13.40	27.70	−9.73	2.77	19.49
$P_{M\to S}$	4.02×10^{-6}	0.0009	0.53	−10.72	1.20	16.58
$P_{S\to T}$	-1.74×10^{-6}	−0.005	0.31	21.66	2.57	2.03

- For normal incident waves and smooth topography, there is little instability and little EKE.
- For normal incident waves and irregular topography, the standing eddies S are unstable and transfer energy to both the alongshore mean flow M and the transient eddies T.
- For oblique waves and smooth topography, the instability is from M to T with little exchange with S.
- For oblique waves and irregular topography, M is strongly unstable to S, and the conversions to T are moderate.

3.4. Wave energy

Because of CEW the wave field is modulated by interactions with the current as well as with the variable topography. Previous rip-current Yu and Slinn (2003) and Weir et al. (2011) show how CEW weakens the rip currents and their instability especially for smaller values of θ by comparing with solutions in which CEW is neglected. Here all solutions include CEW through full wave–current coupling (Section 2.1). The results discussed below are not shown since the all the cases (smooth and irregular barred topography cases) exhibit similar behavior.

We first discuss the alongshore- and time-averaged sea-level and significant wave height. Crossing the bar the waves begin to break and dissipate, and the sea-level rises shoreward as wave setup (Longuet-Higgins and Stewart, 1962). There is a modest indication of wave setdown and amplification just offshore of the bar. A secondary round of breaking and setup occurs close to the shore at $x \approx 1$ m depth. In a broad view all cases have similar behavior, although the irregular topographies induce somewhat greater dissipation and setup.

Next, we discuss the wave energy for all the smooth and irregular barred topographies. Wave energy is calculated from the linear wave theory at leading order in wave steepness. The time averaged wave energy for all barred topography cases shows a broad pattern of E_w decreasing shoreward from the bar. There is also evident modulation of the waves in the irregular topography cases. For $\theta \geq 20°$, the magnitude of E_w is similar for both smooth and irregular cases. For

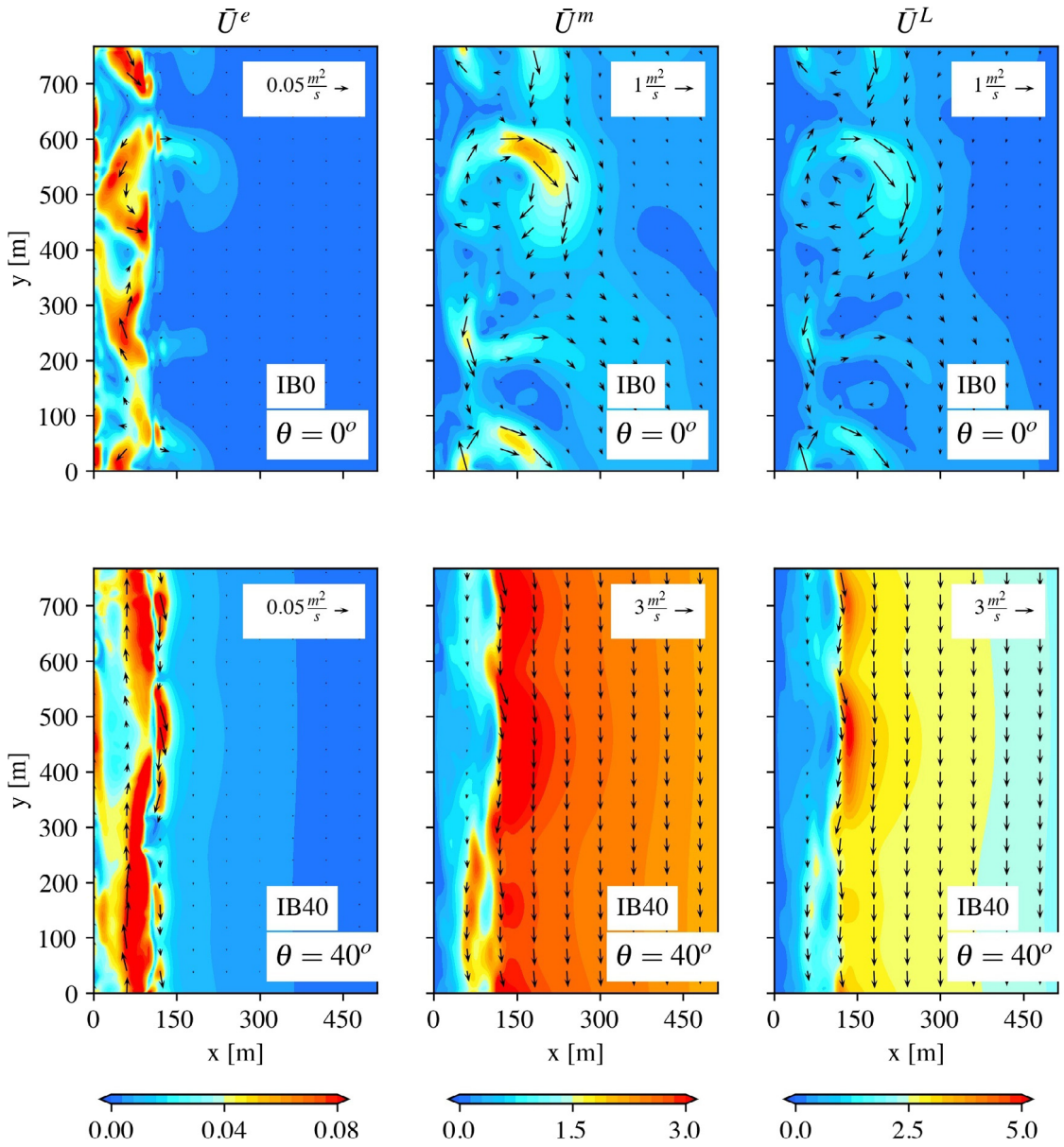

Fig. 10. Maps of time-averaged and depth-integrated transport components [$m^2\ s^{-1}$]: eddy-induced $\mathbf{U}^e$ (left panels), mean $\mathbf{U}^m$ (middle panels), and total Lagrangian mean $\mathbf{U}^L$ (right panels) for irregular barred topography with $\theta = 0°$ (case IB0; top panels) and $\theta = 40°$ (case R20; bottom panels). Arrows denote transport vectors, and colors indicate magnitudes.

$\theta < 20°$, highest wave energy is seen where the rip channels are located (*i.e.,* in this h' realization, at ≈ 80 m, 200 m, and 600 m in the alongshore and ≈ 120 m in the cross-shore direction). These are sites of wave amplification and enhanced dissipation partly through the CEW associated with the offshore rip currents there.

3.5. Horizontal transport

The Lagrangian horizontal volume transport (or mass flux when multiplied by ρ_0 in this Boussinesq model) is defined as

$$\mathbf{U}^L = \int_{-h}^{\eta_c} (\mathbf{u} + \mathbf{u}^{st})\, dz = H\mathbf{u}_{bt} + \mathbf{U}^{st}. \tag{11}$$

$\mathbf{u}_{bt}$ is the depth-averaged (barotropic) velocity, and $\mathbf{U}^{st}$ is the depth-integrated Stokes transport (Uchiyama et al., 2010). When time-averaged, the Lagrangian mean transport is

$$\begin{aligned}\overline{\mathbf{U}^L} &= \overline{H'\mathbf{u}'_{bt}} + \bar{H}\,\bar{\mathbf{u}}_{bt} + \bar{\mathbf{U}}^{st} \\ &= \bar{\mathbf{U}}^e + \bar{\mathbf{U}}^m + \bar{\mathbf{U}}^{st},\end{aligned} \tag{12}$$

where the first right-side term is the mean eddy-induced Eulerian transport, the second term is the Eulerian transport by the mean flow, and the last term is the Stokes transport. The second right-side line in (12) is a more compact notation for the terms in the first line. Notice that the occurrence of surf eddies allows for there to be "eddy" contributions to eddy-induced mean flow, the familiar one from surface gravity waves, $\bar{\mathbf{U}}^{st}$, and another from the rectified transport by surf eddies, $\bar{\mathbf{U}}^e$.

In the context of oceanic mesoscale eddy material fluxes, the isopycnal-layer thickness-weighted eddy-induced transports are a significant element in general circulation dynamics (Gent et al., 1995). The dynamical processes that generate these different types of eddy-induced transport are different, of course, and as yet there is no clear explanation for this surf eddy manifestation.[3]

[3] It is well known that shallow-water gravity waves generate a non-zero Stokes transport, but in our incident-wave-averaged ROMS-WEC model, the solutions in our present cases exhibit relatively weak infra-gravity wave behavior, so here $\mathbf{U}^e \neq 0$ is due mainly to surf eddy dynamics.

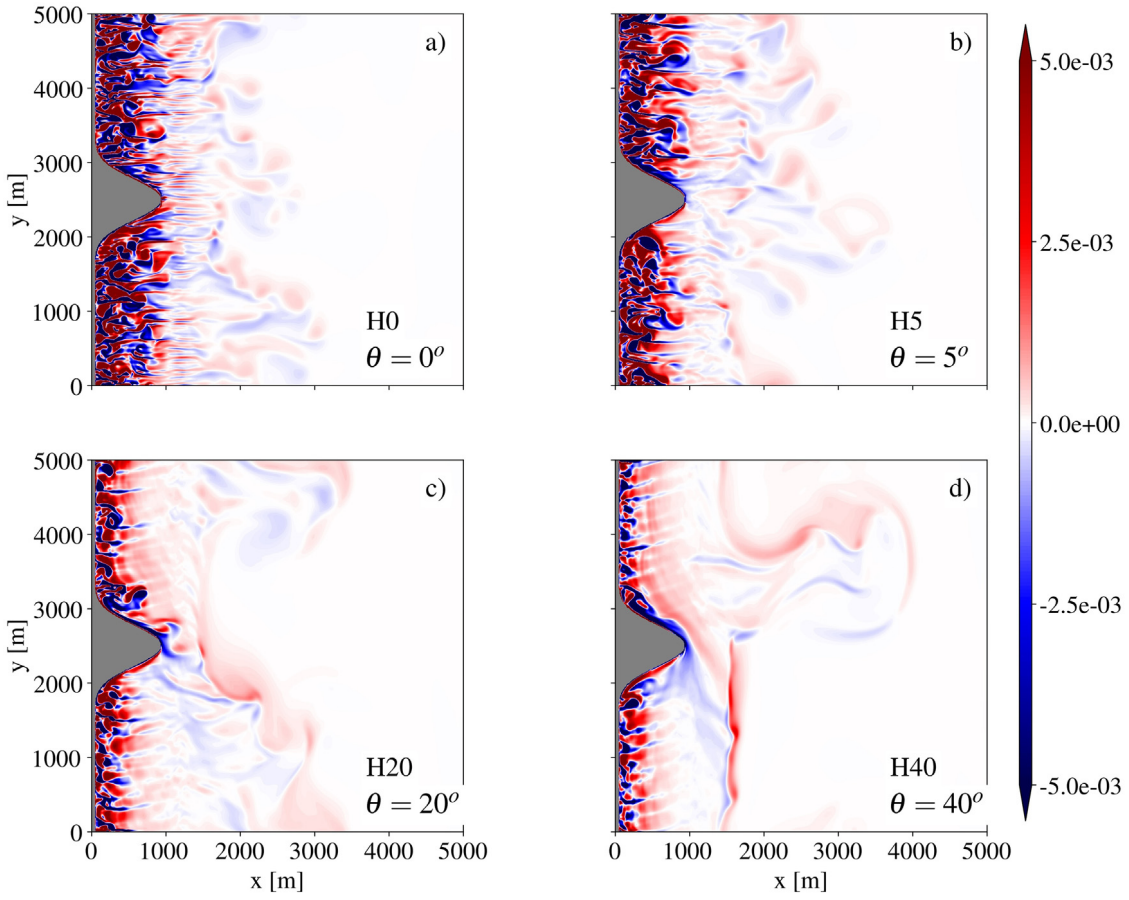

Fig. 11. Instantaneous surface vertical vorticity $\zeta_z^s(x, y)$ $[s^{-1}]$ in the headland cases with irregular topography and incident wave angles of (a) $\theta = 0°$ (case H0), (b) $\theta = 5°$ (case H5), (c) $\theta = 20°$ (case H20), and (d) $\theta = 40°$ (case H40) at the 24th hour of the simulation.

Following Yu and Slinn (2003), we examine the transport in the x-direction associated with the rip currents as the alongshore average of the positive portion of the depth- and time-averaged $(U^m + U^e)_+$ which is shown in Fig. 9.[4] There are striking differences between the cases. First, the net rip transport is quite small for all the smooth barred topography cases, even though it can be locally large due to transient surf eddies. With irregular topography it is much larger, but somewhat it decreases with θ, especially in comparing normal- and oblique-incident cases. This is consistent with decreasing EKE with θ (Fig. 4). Yu and Slinn (2003) report a similar pattern in their simulations with uniformly-spaced rip-channel topography. In our cases, we generated topographies that are random in the alongshore direction. Here, we see an across-shore transport that is much stronger and extends much further than in their simulations. This indicates that irregular topography is significant in transporting materials offshore. However, it should be also noted that the present study does not take into account the type of wave breaking (spilling/plunging) which also impacts the direction of transport of materials in the surf zone.

The components of mean transport in (12) are shown in Fig. 10 for irregular barred topography. This shows an eddy-induced transport directed primarily alongshore in the surf zone, with a direction-reversing pattern in y. For normal-incident waves, the eddy and mean transport components show some recirculations (observe the direction of the transport vectors). On the other hand, for oblique waves the eddy and mean transport components are aligned along the shore. The magnitude of $\bar{\mathbf{U}}^e$ is smaller than $\bar{\mathbf{U}}^m$; where it is largest in the surf zone, its peak value is only 5%–10% as large. For smooth barred topography (not shown), $\bar{\mathbf{U}}^m$ is very small for normal waves (because there is little transient eddy activity), and it has a comparable relative size for oblique waves. For oblique waves the total transport offshore is southward in the direction of the waves. The transport due to the Stokes drift is comparable in magnitude to the eddy-induced transport in these irregular topography cases with a straight coastline, but with a very different spatial pattern (n.b., Fig. 6).

In an additional alongshore average, we can further decompose the mean transport by separating standing and transient eddies,

$$\begin{aligned}\langle\overline{\mathbf{U}^L}\rangle &= \langle\overline{H'\mathbf{u}'_{bt}}\rangle + \langle H^s\mathbf{u}^s_{bt}\rangle + \langle\bar{H}\rangle\langle\bar{\mathbf{u}}_{bt}\rangle + \langle\bar{\mathbf{U}}^{st}\rangle \\ &= \langle\mathbf{U}^{TE}\rangle + \langle\mathbf{U}^{SE}\rangle + \langle\mathbf{U}^{M}\rangle + \langle\bar{\mathbf{U}}^{st}\rangle, \end{aligned} \tag{13}$$

where the definitions should be evident from the symbols. For the same solutions as in Fig. 9 with irregular topography, $\langle\mathbf{U}^{TE}\rangle$ is again about 4% of $\langle\mathbf{U}^{M}\rangle$ for normal-incident waves, while the relative magnitude of $\langle\mathbf{U}^{SE}\rangle$ is close to 35%. For oblique waves $\langle\mathbf{U}^{TE}\rangle$ and $\langle\mathbf{U}^{SE}\rangle$ are each about 10% as large as $\langle\mathbf{U}^{M}\rangle$ within the surf zone (inner 100 m in x), but smaller farther offshore. Thus, the surf-eddy-induced mean transports are non-trivial in these cases, although the primary transport is by the mean currents.

4. Effects of coastline shape

The usual practice in idealized rip-current studies is to have a straight coastline, and as far as we know most field measurements in the surf have been measured for a similar geometry. In this section we examine the influence of a variable shoreline on generating and interacting with rip currents. As explained in Section 2, the topographies of the headland and bay cases are sloped downward and seaward with superimposed random depth perturbations; *i.e.,* there are no bars in these cases. In this section we do not consider alongshore averages because of the inhomogeneity in this direction.

[4] Subscript "+" denotes average of the positive portion.

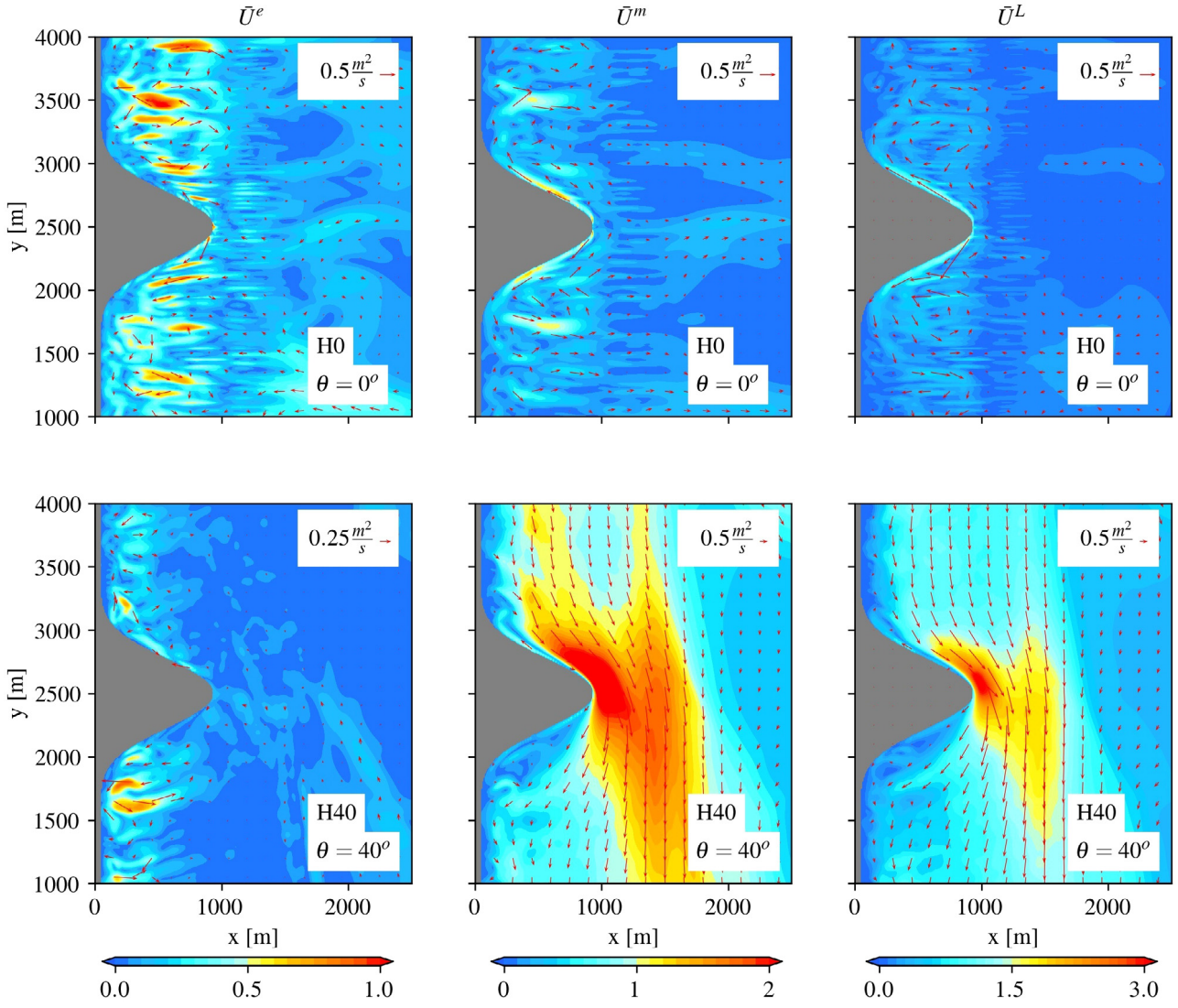

Fig. 12. Maps of time-averaged and depth-integrated transport components [m^2 s^{-1}]: eddy-induced $\mathbf{U}^e$ (left panels), mean-current $\mathbf{U}^m$ (middle panels), and total-Lagrangian $\mathbf{U}^L$ (right panels) for a headland with irregular topography and with $\theta = 0°$ (case H01; top panels) or $\theta = 40°$ (case H40; bottom panels). Arrows denote transport vectors and colors indicate magnitudes.

4.1. Headlands

The surface vertical vorticity around the headland for different incident waveangles at the 24th hour of the simulation is illustrated in Fig. 11. Highly energetic small-scale surf eddies are generated along the straight sectors of the coastline with normal and nearly normal-incident wave angles. They persist for all incident angles but weaken and contract shoreward with larger θ. The surf eddies on both sides of the headland are suppressed. In addition, for $\theta \geq 20°$, a strong alongshore current develops on the wave-exposed side of the headland, with strong nearshore negative surface vertical vorticity due to increased bottom drag in shallow water. This flow separates at the headland, leaving the wave-sheltered side relatively inactive (not evident from the figures). Because it is a wave-driven current shaped by the irregular domain geometry, we refer to it as a mega-rip current. It extends seaward far beyond the surf zone where the waves break.

To understand the transport around the headland, we again utilize the transport decomposition (12). Components of the transport and their sum at different incident wave angles are shown in Fig. 12. When the waves are normally incident (top panels), in addition to the local irregular-topography standing eddies in the surf zone, we see two large circulating patterns in the regions next to the headland. Right around the headland, the transport is negative (*i.e.,* directed towards shore), and away from the headlands there is a compensating offshore flow. The relative size of $\mathbf{U}^e$ compared to $\mathbf{U}^m$ is larger in this headland case than with a straight coastline (Section 4), *i.e.,* as large as about 50% (based on the maximum in one computational cell) locally within the surf zone. When the waves are obliquely incident (bottom panels), the transport is mainly directed along the incident wave direction towards south, with an especially strong separating flow at the headland tip. In this case the eddy-induced flows are positioned differently and are somewhat weaker compared to the mean-current transport.

4.2. Bays

Fig. 13 is an analogous illustration of the surface vertical vorticity around the bay for different incident wave angles at the 24th hour of the simulations. Along the straight sectors of the coast the behavior of the small surf eddies is quite similar to that for the headland (Fig. 11). A striking feature in these cases is the mega-rips extending far offshore. Around the bay the mega-rip pattern is broadly a dipole with inflows at the bay edges and a central outflow. The dipole is approximately symmetric with normal incident waves, but it is tilted alongshore with oblique waves in the wave direction. The offshore-directed flow from

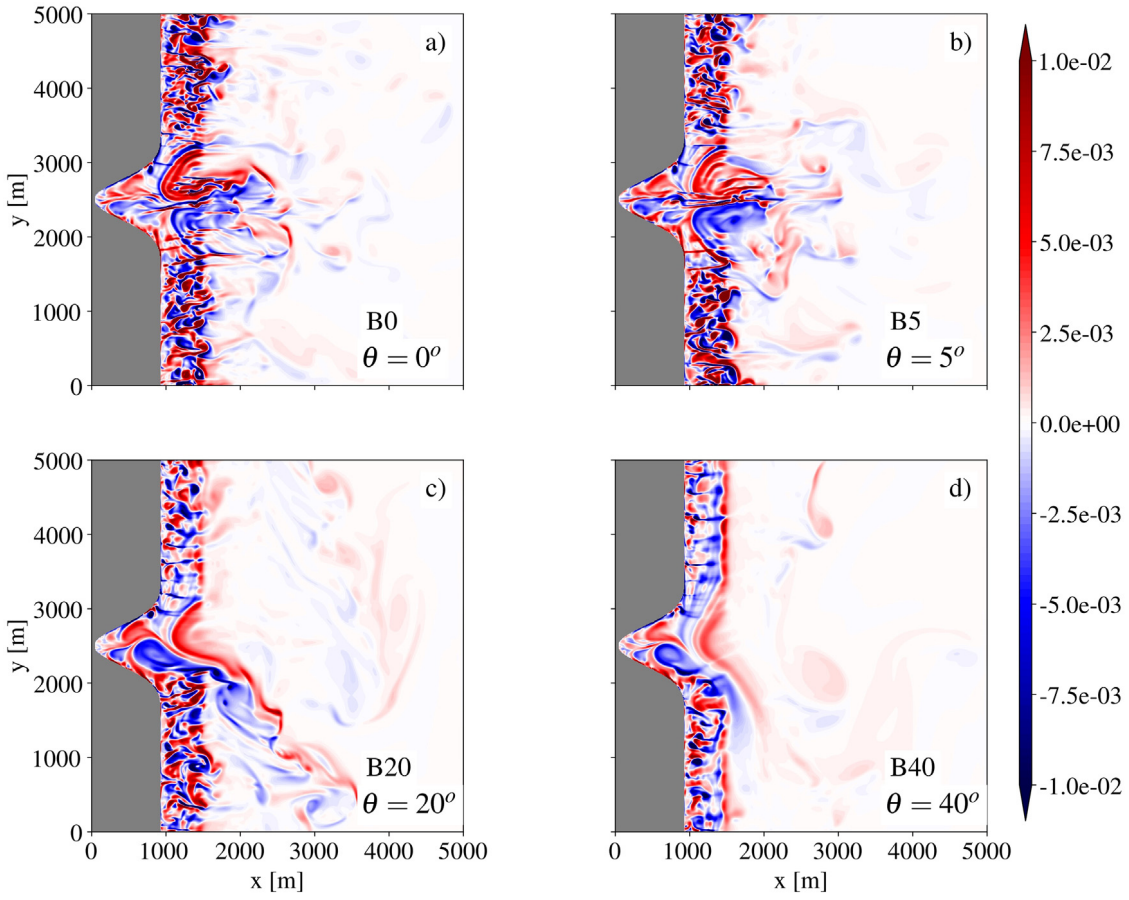

Fig. 13. Instantaneous surface vertical vorticity $\zeta_z^s(x, y)$ $[s^{-1}]$ in the bay cases with irregular topography and incident wave angles of (a) $\theta = 0°$ (case B0), (b) $\theta = 5°$ (B5), (c) $\theta = 20°$ (B20), and (d) $\theta = 40°$ (B40) at the 24th hour of the simulation.

the bay center is shear-unstable and tends to meander around its primary axis. Similar mega-rips were observed around a submarine canyon off La Jolla, CA, near the Scripps Research Pier, which is much deeper than our idealized bay (30–40 m); Long and Özkan Haller (2005) studied the mega-rip generated at this location and reported that rip current generation was very sensitive to the topographic irregularities rather than presence of the canyon. We did not repeat our simulation without the h perturbations, but based on the results in the previous section, we would expect a similar result that irregularness enhances variability here. The mega-rip interacts with the smaller rip currents for all of the incident wave angles. This implies that materials transported by the smaller rip currents would be transported even further offshore through this interaction with the mega-rip circulation.

Fig. 14 shows the transport around the bay for different incident wave angles. The eddy-induced flow patterns generated due to the bay are stronger, more complicated, and extend farther offshore than in the headland cases, but again its magnitude relative to the mean-current transport is larger than with only a straight coastline (Fig. 12). The transport direction is affected significantly because of the mega-rip. The mean-current and total-Lagrangian alongshore transports are enhanced by the presence of the bay and are strongest while exiting on the down-wave side.

In the headland and bay cases with relatively larger eddy-induced transports compared to straight coastline cases (Fig. 12), the Stokes transport is smaller than the eddy-induced transport. Thus, variations in coastline shape have an important influence on wave-driven currents and surf eddies. The variety of shapes in nature is large, and here we only show two examples to illustrate the influences.

5. Summary and discussion

In this paper we present results from 52 idealized cases for wave-driven surf currents over various topographies and coastline shapes using the ROMS-WEC model (Uchiyama et al., 2010). The cases are divided into two case groups where, in the first group, we investigate topographic control on transient rip currents by introducing irregularities to commonly used alongshore-uniform topographies; in the second group idealized headland and bay domains with topographic irregularities are examined for their influences on transient rip currents. In both groups the role of the incident wave angle is examined, while the other incident wave properties are held constant.

The results from the first group show that if the topography in the alongshore direction has irregular undulations, instabilities are triggered even at normally incident wave angles. With increasing incident angle, shear instabilities dominate over topographic instabilities, and the surf eddies transition from being mostly transient to being mostly steady. The surf EKE is enhanced by the presence of irregular topography. This enhancement is greatest for nearly normal incidence, which is the attracting direction for depth-induced refraction over shoaling bathymetry.

The second-group cases with idealized headland and bay configurations reveal how the flow field changes when the coastline shape changes. The headland acts like an obstruction especially at high incident wave angles, and we observe flow separation followed by offshore wake instabilities. The bay, however, acts like a large rip channel generating transient mega-rips with large-scale recirculating flow patterns that intrude out from the coast several kilometers offshore when the waves are normally incident.

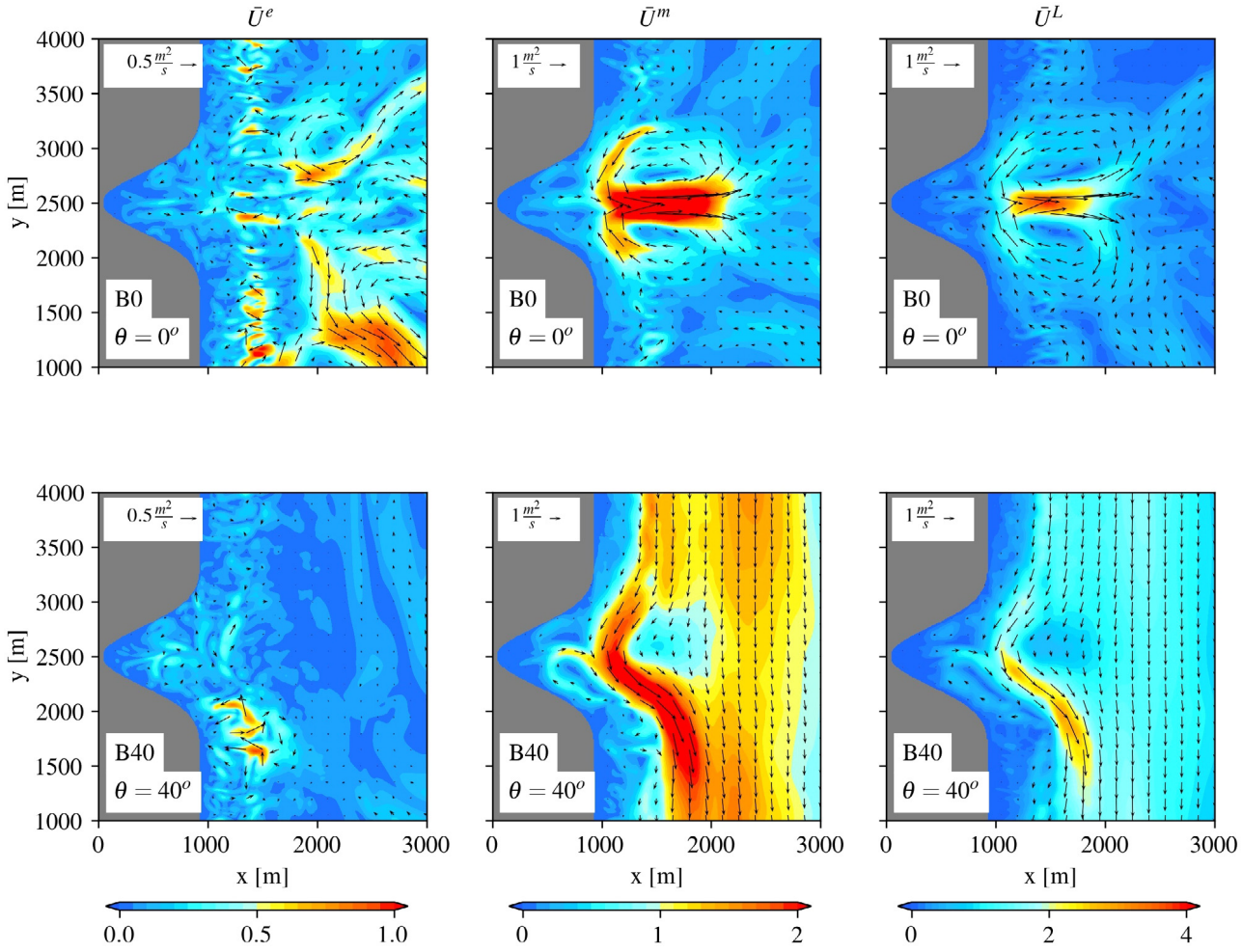

Fig. 14. Maps of time-averaged and depth-integrated transport components [$m^2\ s^{-1}$]: eddy-induced $\mathbf{U}^e$ (left panels), mean-current $\mathbf{U}^m$ (middle panels), and total-Lagrangian $\mathbf{U}^L$ (right panels) for a headland with irregular topography and with $\theta = 0°$ (case B0; top panels) or $\theta = 40°$ (case B40; bottom panels). Arrows denote transport vectors and colors indicate magnitudes.

In flows with significant transient eddies, an eddy-induced mean transport often occurs and can be large in relation, *e.g.,*to the mean Stokes transport. It also often provides a fractional opposition to the mean-current transport that dominates the total Lagrangian transport. The eddy-induced transport is enhanced by irregular topography, just as is the EKE.

These eddy-induced transports are modest fractions of the mean-current and total transports in the idealized cases with straight coastline and relatively small-scale topographic irregularities, and they are relatively stronger with coastline shape variations. Nevertheless, they do demonstrate the potential importance of surf turbulence in providing a Lagrangian-mean advective material transport as well as the more familiar behaviors of eddy-induced dispersion and dilution of material concentrations.

The results of this study demonstrate that topographic and coastline variations are significant influences on surf eddy activity. Thus, for realistic surf behaviors it is important to use either measured bathymetry, if available, or at least include a plausible degree of irregularity and coastline variation in the simulation. Beyond the steady wave forcing considered here, both incident wave variability and other forms of shelf-current variability are also necessary ingredients for realistic surf eddy simulations.

Finally, it should be noted that the currents in the surf zone can also further be influenced by tidal forces, large (oceanic) scale thermohaline differences and river discharges. Moreover, truly irregular wave fields with special dynamics (EKE, surface vertical vorticity, velocity fields) induced by realistic random wave trains could be achieved only by coupling ROMS with proper wave models (3rd generation or Boussinesq-type) and CFD approaches, so that other crucial wave processes can be incorporated in simulations, such as wave triad interactions, wave reflections on the coast, surf beat, cross-shore wave dynamics, wave run-up/run-down on the coastal boundary.

Declaration of competing interest

The authors declare that they have no known competing financial interests or personal relationships that could have appeared to influence the work reported in this paper.

CRediT authorship contribution statement

Çiğdem Akan: Conceptualization, Methodology, Software, Data curation, Writing - original draft, Visualization, Investigation. **James C. McWilliams:** Supervision, Writing- reviewing & editing. **Yusuke Uchiyama:** Writing - reviewing & editing.

Acknowledgments

This research is supported by the National Science Foundation (OCE-1355970) and the Office of Naval Research (N00014-14-1-0626

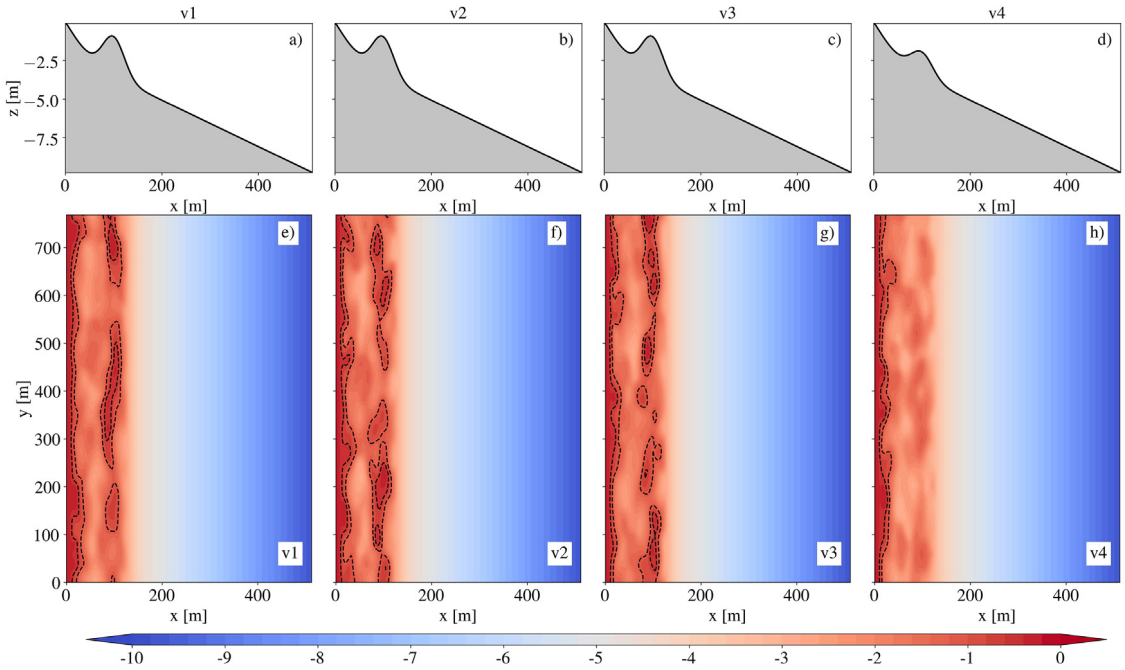

Fig. A.1. Alongshore averaged (a–d) and horizontal (f–h) views of different realizations of the barred topography generated by the method described in Section 2.2. Case v1 is the same as the irregular barred topography used in cases IB0 through IB40. Cases v1–v3 are different random realizations with the same bar profile, and case v4 is a realization with a bar whose top is deeper.

and N00014-15-1-2645), as well as by the Extreme Science and Engineering Discovery Environment (XSEDE) computational resources. YU receives financial support for a sabbatical visit to UCLA from the JSPS Grants-in-Aid for Scientific Research (Grant Numbers: 15KK0207 and 15H04049) at Kobe University.

Appendix A. Sensitivity to random realizations

We follow the procedure explained in Section 2.2 and generate two more random realizations of the topographic perturbations $h'(x, y)$, which then are superimposed on the alongshore-uniform barred topography (Fig. A.1). Time histories of the instantaneous eddy kinetic energy (*i.e.,* $EKE(t)$, calculated using the eddy velocity $\mathbf{u} - \langle\mathbf{u}\rangle$) are shown in Fig. A.2 for these three realizations: v1 is the "control" case (SB0), and v2 and v3 are two other random realizations. Otherwise, all parameters for the three cases are the same. (Notice that, v4 is not included in Fig. A.2 and will be discussed in Appendix B.) The $EKE(t)$ varies over a 50% range, but the different cases' curves overlap substantially with each other and have a similar time average. This implies that repeating the simulations given in Table 1 with different realizations would yield in similar statistical results. Because the size and location of the rip channels are different in each case, the detailed pattern of the rip currents would be different, but the results leading to our conclusions would be essentially similar.

Appendix B. Sensitivity to bar height

We examine the time series of EKE components (standing and transient) for different barred topography realizations. We use four cases where when alongshore averaging applied, the height of the bar in v1, v2 and v3 is the same whereas the bar top is deepened in v4. The components of the EKE and its total decline when the bar top is deepened. However, the transient EKE component is noticeably larger for large θ with the deepened bar and relatively weak transient eddies are observed at large incident angle.

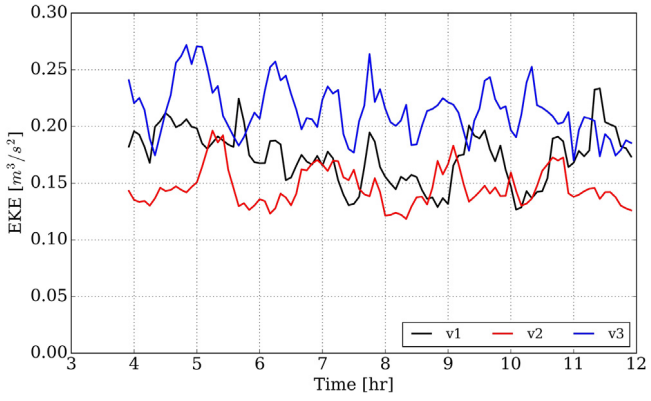

Fig. A.2. Time series of EKE for different realizations of the barred topographies in cases v1–v3 in Fig. A.1. The incident angle is $\theta = 0°$.

Appendix C. Sensitivity to roughness factor s_0

Here we vary s_0 between 1 and 0, where 1 yields the full perturbation amplitude in (5), to assess how the topographic irregularness amplitude controls the surf eddy activity. As expected and consistent with the results in Uchiyama et al. (2017), smaller perturbation size led to lower EKE and therefore less energetic flow field with less instabilities.

Appendix D. Sensitivity to wave amplitude a

Now we vary the offshore wave amplitude a and plot the resulting EKE values (Fig. D.1. For small a the rate of increase in EKE is large, but there is a saturation effect for larger a, *i.e.,* increased incident wave energy, hence increased wave dissipation and current acceleration, lead to increased current dissipation such that EKE does not increase further.

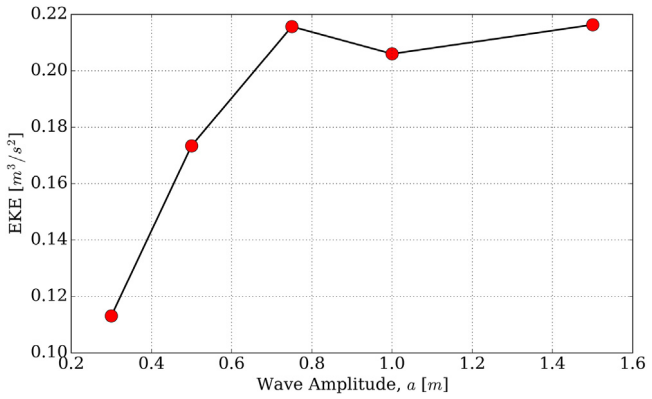

Fig. D.1. EKE for different incident wave amplitudes. These are IB0-type cases with barred irregular topography and $\theta = 0°$.

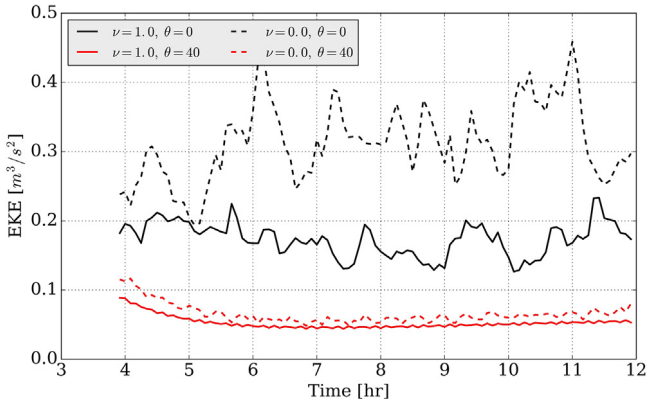

Fig. E.1. Time series of depth-integrated EKE [$m^3\ s^{-1}$] for different values of lateral eddy viscosity in cases with barred irregular topography and $\theta = 0°$ or $40°$.

Appendix E. Sensitivity to horizontal viscosity ν

As a final sensitivity test we compared solutions with irregular barred topography and a straight coastline using the standard lateral momentum eddy viscosity of $\nu = 1\ m^2\ s^{-1}$ and the alternative value of zero. In both cases the third-order upstream horizontal advection provides an implicit hyper-diffusion that adapts to both the grid and the flow; in extensive experience with ROMS, this implicit diffusion is often sufficient to maintain smoothness on the grid scale (Shchepetkin and McWilliams, 2005). Results are shown in Fig. E.1. As expected, the explicit $\nu \neq 0$ is unnecessary for stability, and the EKE is enhanced without it. The enhancement is more substantial for normal-incident waves than oblique waves, because the ensuing surf turbulence in the former case has a wider range of scales and a more active kinetic energy cascade (Fig. 3). Thus, our conclusion about topographic enhancement of surf eddy activity would be even stronger with smaller ν.

Bennis et al. (2011) reported that CEW will be diminished for ν values greater than $2.5\ m^2\ s^{-1}$ and the ν value used in the present study is 2.5 times smaller than this limit.

Appendix F. Eddy-mean induced transport & mean Stokes drift comparison with varying wave amplitude

Finally, we examined the effect of wave amplitude on eddy-mean induced transport and mean Stokes drift which is shown in Fig. F.1. Eddy-mean induced transport is highest onshore after the bar for all cases as expected. Eddy-mean transport shows an increasing trend with increasing wave amplitude with the exception for $a = 0.25$ and $a = 0.5$. $\bar{\mathbf{U}}^e$ with $a = 0.5$ is much smaller than the $\bar{\mathbf{U}}^e$ with $a = 0.25$ for $x < 150$ m.

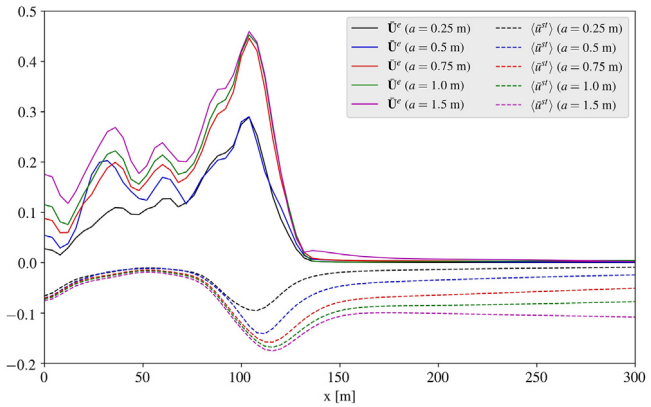

Fig. F.1. Time and alongshore averaged and depth-integrated eddy-mean induced transport, $\bar{\mathbf{U}}^e$, (solid lines) and depth-, time, and alongshore-averaged Stokes drift, $\langle \bar{u}^{st} \rangle$, (dashed lines) for varying wave amplitudes for irregular barred topography.

For $a \geq 0.75$ the peak values of $\bar{\mathbf{U}}^e$ are indistinguishable whereas mean Stokes drift keeps increasing with increasing wave amplitude.

References

Apotsos, A., Raubenheimer, B., Elgar, S., Guza, R.T., 2008. Testing and calibrating parametric wave transformation models on natural beaches. Coastal Eng. 55, 224–235.

Bennis, A.-C., Dumas, F., Blanke, B., 2011. Modulation of wave–current interactions by horizontal mixing and spatial resolution. Ocean Model. 99, 75–85.

Bruneau, N., Bonneton, P., Castelle, B., Pedreros, R., 2011. Modeling rip current circulations and vorticity in a high-energy mesotidal-macrotidal environment. J. Geophys. Res. 116, C07026.

Castelle, B., Reniers, A., MacMahan, J., 2014. Bathymetric control of surf zone retention on a rip-channelled beach. Ocean Dyn. 64 (8), 1221–1231.

Castelle, B., Scott, T., Brander, R.W., McCarroll, R.J., 2016. Rip current types, circulation and hazard. Earth-Sci. Rev. 163, 1–21.

Crossett, K., Ache, B., Pacheco, P., Haber, K., 2013. National Coastal Population Report: Population Trends from 1970 to 2020. NOAA's State of the Coasts, http://oceanservice.noaa.gov/facts/coastal-population-report.pdf. (Accessed January 2017).

Dalyrmple, R.A., MacMahan, J.H., Reniers, A.J.H.M., Nelko, V., 2011. Rip currents. Annu. Rev. Fluid Mech. 43, 551–581.

Evensen, G., 2007. Data Assimilation: The Ensemble Kalman Filter. Springer, p. 279.

Feddersen, F., Clark, D.B., Guza, R.T., 2011. Modeling surf zone tracer plumes: 1. waves, mean currents, and low-frequency eddies. J. Geophys. Res. 116, C11027.

Feddersen, F., Guza, R.T., Elgar, S., Herbers, T., 2000. Velocity moments in alongshore bottom stress parameterizations. J. Geophys. Res. 105, 8673–8686.

Fewings, M., Lentz, S.J., Fredericks, J., 2008. Observations of cross-shelf flow driven by cross-shelf winds on the inner continental shelf. J. Phys. Oceanogr. 38, 2358–2378.

Gent, P.R., Willebrand, J., McDougall, T.J., McWilliams, J.C., 1995. Parameterizing eddy-induced tracer transports in ocean circulation models. J. Phys. Oceanogr. 25, 463–474.

George, D.A., 2016. Circulation and Sediment Transport At Headlands with Implications for Littoral Cell Boundaries (PhD diss). University of California, Davis.

Haas, K.A., Svendsen, I.A., Haller, M.C., Zhao, Q., 2003. Quasi three-dimensional modeling of rip current systems. J. Geophys. Res. 108, 3217.

Haller, M.C., Honegger, D., Cataln, P.A., 2014. Rip current observations via marine radar. J. Waterw. Port C.-ASCE 140, 115–124.

Özkan Haller, H.T., Li, Y., 2003. Effects of wave–current interaction on shear instabilities of longshore currents. J. Geophys. Res. Ocean. 108, 3139.

Long, J.P., Özkan Haller, H.T., 2005. Offshore controls on nearshore rip currents. J. Geophy. Res. 110, C12007.

Longuet-Higgins, M.S., Stewart, R.W., 1962. Radiation stress and mass transport in gravity waves, with application to 'surf beats'. J. Fluid Mech. 13, 481–504.

MacMahan, J.H., Reniers, A.J.H.M., Thornton, E.B., Stanton, T.P., 2004. Surf zone eddies coupled with rip current morphology. J. Geophy. Res. 109, C07004.

Marchesiello, P., Almar, R., Benshila, R., Larnier, S., Castelle, B., McWilliams, J.C., 2016. Eddy mixing of longshore currents: Video observation and 3D modeling of Grand Popo beach. Benin. J. Coast. Res. 75, 408–412.

Marchesiello, P., Benshila, R., Almar, R., Uchiyama, Y., McWilliams, J.C., Shchepetkin, A., 2015. On tridimensional rip current modeling. Ocean Model. 96, 36048.

McWilliams, J.C., Restrepo, J.M., Lane, E.M., 2004. An asymptotic theory for the interaction of waves and currents in coastal waters. J. Fluid Mech. 511, 135–178.

National Weather Service, 2016. Summary of natural hazard statistics for 2015 in the united states.

Shchepetkin, A., McWilliams, J.C., 2005. The regional oceanic modeling system (ROMS): a split-explicit, free-surface, topography-following-coordinate oceanic model. Ocean Model. 9, 347–404.

Soulsby, R.L., 1995. Bed shear-stresses due to combined waves and currents. In: Stive, M.J.F., et al. (Eds.), Advances in Coastal Morphodynamics. Delft Hydraulics, Delft, Netherlands, pp. 4–20–4–23.

Thornton, E.B., Guza, R.T., 1983. Transformation of wave height distribution. J. Geophys. Res. 88, 5929–5938.

Uchiyama, Y., McWilliams, J.C., Akan, C., 2017. Three-dimensional transient wave-driven currents: Low-frequency variability in alongshore and rip currents. J. Geophys. Res. 122, 2017JC013005.

Uchiyama, Y., McWilliams, J.C., Restrepo, J.M., 2009. Wave-current interaction in nearshore shear instability analyzed with a vortex force formalism. J. Geophys. Res. Ocean. 114, C06021.

Uchiyama, Y., McWilliams, J.C., Shchepetkin, A.F., 2010. Wave-current interaction in an oceanic circulation model with a vortex force formalism: Application to the surf zone. Ocean Model. 34, 16–35.

Weir, A., Uchiyama, Y., Lane, E.M., Retrepo, J.M., McWilliams, J.C., 2011. A vortex force analysis of the interaction of rip currents and gravity waves. J. Geophys. Res 116, C050011.

Xie, M., 2011. Validation and discussions of a three dimensional wave-induced current model. Ocean Model. 38 (3), 230–243.

Yu, J., Slinn, D.N., 2003. Effects of wave–current interaction on rip currents. J. Geophys. Res. 108, 3088.